SMARCE1 deficiency generates a targetable mSWI/SNF dependency in clear cell meningioma

St Pierre, Roodolph; Collings, Clayton K.; Guerra, Daniel D. Same; Widmer, Christian J.; Bolonduro, Olubusayo; Mashtalir, Nazar; Sankar, Akshay; Liang, Yu; Bi, Wenya Linda; Gerkes, Erica H.

Published in:
Nature genetics

DOI:
10.1038/s41588-022-01077-0

Publication date:
2022

nature genetics

ARTICLES

https://doi.org/10.1038/s41588-022-01077-0

SMARCE1 deficiency generates a targetable mSWI/SNF dependency in clear cell meningioma

Roodolph St. Pierre[1,2,3,11], Clayton K. Collings[1,2,11], Daniel D. Samé Guerra[1,2], Christian J. Widmer[1,2], Olubusayo Bolonduro[1,2], Nazar Mashtalir[1,2], Akshay Sankar[1,2], Yu Liang[4], Wenya Linda Bi[5], Erica H. Gerkes[6], Vijaya Ramesh[7], Jun Qi[4], Miriam J. Smith[8,9], David M. Meredith[10] and Cigall Kadoch[1,2] ✉

Mammalian SWI/SNF (mSWI/SNF) ATP-dependent chromatin remodeling complexes establish and maintain chromatin accessibility and gene expression, and are frequently perturbed in cancer. Clear cell meningioma (CCM), an aggressive tumor of the central nervous system, is uniformly driven by loss of SMARCE1, an integral subunit of the mSWI/SNF core. Here, we identify a structural role for SMARCE1 in selectively stabilizing the canonical BAF (cBAF) complex core–ATPase module interaction. In CCM, cBAF complexes fail to stabilize on chromatin, reducing enhancer accessibility, and residual core module components increase the formation of BRD9-containing non-canonical BAF (ncBAF) complexes. Combined attenuation of cBAF function and increased ncBAF complex activity generates the CCM-specific gene expression signature, which is distinct from that of NF2-mutated meningiomas. Importantly, SMARCE1-deficient cells exhibit heightened sensitivity to small-molecule inhibition of ncBAF complexes. These data inform the function of a previously elusive SWI/SNF subunit and suggest potential therapeutic approaches for intractable SMARCE1-deficient CCM tumors.

The dynamic control of genomic accessibility is required for timely and appropriate gene expression, and is achieved in part by the activity of ATP-dependent chromatin remodeling complexes[1]. These complexes utilize the energy of ATP hydrolysis to alter DNA–nucleosome contacts on chromatin, thereby modulating local chromatin architecture. One such family of remodelers, the mSWI/SNF (or BAF) family, is comprised of three main complexes, termed cBAF, polybromo-associated BAF (PBAF) and ncBAF, and within these, hundreds of different variants owing to the incorporation of paralog subunits[2,3].

The genes encoding mSWI/SNF complexes are mutated in over 20% of human cancers, with some subunit genes mutated across a wide range of cancer types and others in highly cancer-specific contexts[4–6]. For example, >98% of malignant rhabdoid tumor and atypical teratoid/rhabdoid tumors bear *SMARCB1* mutations, ~100% of synovial sarcoma tumors contain the hallmark SS18–SSX fusion oncoprotein, and small cell carcinoma of the ovary hypercalcemic type is characterized by dual mSWI/SNF ATPase subunit loss (SMARCA4/SMARCA2 dual deletion)[7–10]. Further, mSWI/SNF mutations are frequent in several adult tumors, including *ARID1A* mutations in ~60% of ovarian clear cell carcinomas and *SMARCA4* mutations in ~11% of nonsmall cell lung cancer, among others[11–13]. One common theme linking these disease contexts is that they nearly all contain perturbations in complex members defining the cBAF complex core structural and functional module[2,14,15], which consists of SMARCA4/2, ARID1A/B, SMARCB1 and SMARCE1 subunits. Although mutations in *SMARCB1*, *ARID1A/B* and *SMARCA4/2* have been studied extensively by our group and others[14,16–19], the role of SMARCE1 remains poorly defined.

SMARCE1 is a ubiquitously expressed mSWI/SNF subunit and is a member of both cBAF and PBAF complexes, but is absent from the ncBAF complex[2,3]. SMARCE1 contains a centrally positioned coiled-coil domain and an N-terminal high-mobility group (HMG) DNA-binding domain. Importantly, recent exome-wide sequencing studies have revealed that mutations in *SMARCE1* cause CCM tumors of both spinal and cranial origin[20–28]. *SMARCE1*-mutant CCM disproportionately affects younger individuals (median age = 11 years) (Supplementary Table 1 and Extended Data Fig. 1a,b). Meningiomas frequently exhibit loss of the tumor suppressor *NF2*; however, *SMARCE1* mutations occur in a mutually exclusive manner, signifying a separate and highly aggressive class of meningiomas[20,21,29–32]. Further, *SMARCE1* mutations do not co-occur with other recurrent mutational events implicated in meningioma biology, such *KLF4*, *TRAF7*, *SMO*, *SUFU*, *SMARCB1* or *PIK3CA* mutations[32] (Extended Data Fig. 1c). Indeed, since the original sequencing efforts identifying *SMARCE1* mutations in the absence of other recurrent mutations[20], it is now known that essentially 100% of CCMs are defined by SMARCE1 loss at the gene and immunohistochemical (protein) levels, implicating aberrant mSWI/SNF function as a driver of this aggressive cancer type[23].

In this study, we integrate biochemical and structural studies with genomics and chemical biology, to uncover a therapeutically relevant set of insights regarding the role for the SMARCE1 subunit in mSWI/SNF function and the biology of CCM.

[1]Department of Pediatric Oncology, Dana-Farber Cancer Institute and Harvard Medical School, Boston, MA, USA. [2]Broad Institute of MIT and Harvard, Cambridge, MA, USA. [3]Chemical Biology Program, Harvard University, Cambridge, MA, USA. [4]Department of Cancer Biology, Dana-Farber Cancer Institute and Harvard Medical School, Boston, MA, USA. [5]Department of Neurosurgery, Brigham and Women's Hospital and Harvard Medical School, Boston, MA, USA. [6]Department of Genetics, University of Groningen, University Medical Center Groningen, Groningen, the Netherlands. [7]Department of Neurology and Center for Genomic Medicine, Massachusetts General Hospital, Boston, MA, USA. [8]Manchester Centre for Genomic Medicine, St Mary's Hospital, Manchester University Hospitals Foundation Trust, Manchester, UK. [9]Division of Evolution, Infection and Genomics, School of Biological Sciences, University of Manchester, Manchester, UK. [10]Department of Pathology, Brigham and Women's Hospital and Harvard Medical School, Boston, MA, USA. [11]These authors contributed equally: Roodolph St. Pierre, Clayton K. Collings. ✉e-mail: Cigall_kadoch@dfci.harvard.edu

Results

SMARCE1 stabilizes the cBAF ATPase and core modules. Mutations occur throughout the *SMARCE1* gene, with the large majority resulting in early truncation and nonsense-mediated decay, leading to complete absence of the SMARCE1 protein (Fig. 1a, Extended Data Fig. 1d and Supplementary Table 1). To biochemically understand the effects of SMARCE1 loss, we generated SMARCE1 knockout (KO) HEK293T cells using CRISPR–Cas9-mediated editing (Fig. 1b,c) and assessed the nuclear abundance and integrity of cBAF and PBAF complexes using immunoprecipitation (IP). Notably, we found that capturing complexes from the SMARCA4 ATPase (and hence, ATPase module) resulted in substantially reduced capture of the cBAF-specific core subunit, ARID1A (which demarcates cBAF complexes), as well as SMARCD2 and SMARCC2, but not in PBAF components such as ARID2 (Fig. 1d). Reciprocally, isolation of ARID1A-bound cBAF complexes, but not ARID2-bound PBAF complexes, showed reduced complex integrity, particularly of the ATPase module components, as well as several members of the initial core (SMARCC2, SMARCD1 and SMARCB1), further demonstrating a cBAF-specific compromise following SMARCE1 loss (Fig. 1e). In parallel, we introduced wild-type (WT) SMARCE1 into a SMARCE1-deficient cancer cell line, BT549, which showed selective cBAF complex stabilization (Extended Data Fig. 1e–g). Finally, density sedimentation studies revealed increased dissociation of cBAF complex components, such as ARID1A and DPF2, as well as SMARCB1, into lower molecular mass fractions of the gradient in the setting of SMARCE1 deletion, indicating a reduced proportion of fully-formed cBAF complexes (Fig. 1f). Similar results were observed in reciprocal experiments in the BT549 SMARCE1-deficient cell line upon SMARCE1 rescue (Extended Data Fig. 1f). Taken together, these findings demonstrate a critical role for SMARCE1 in the stabilization of cBAF but not PBAF complexes.

Structural analyses reveal cBAF-specific SMARCE1 tethering. To understand the biophysical and structural determinants of cBAF-specific disruption mediated by SMARCE1 loss, we performed analyses of cross-linking mass spectrometry (CX-MS) datasets recently generated by our group[2,15] and integrated these results with recent mSWI/SNF three-dimensional (3D) structural studies[15,33–36]. We identified a region of linkage between the SMARCE1 CC domain (amino acids 210–260) and the core module subunits SMARCC1/2 and SMARCD1/2 that was found to be equally enriched on SMARCE1 in both cBAF and PBAF complex contexts (Fig. 2a and Supplementary Table 2). In addition, we observed a linkage region between SMARCE1 and other BAF complex subunits in the region C-terminal to the HMG DNA-binding domain (amino acids 140–170) that was found only in cBAF complexes (Fig. 2a and Extended Data Fig. 2a–c). Notably, cross-links in this region, termed the BAF core binding region (CBR), were detected between SMARCE1 and ARID1A/B subunits of cBAF, but not with the ARID2 subunit of PBAF or other PBAF subunits, despite equal numbers of available lysine residues (Fig. 2a and Extended Data Fig. 2d). SMARCE1–ARID1A cross-links localized to the CBR, which is located in the C terminus in ARID1A/B but in the N terminus in ARID2 (Extended Data Fig. 2d)[2]. Cross-links were enriched for ARID1A binding at positions K146 and K166 of SMARCE1 (Fig. 2a), with additional subunits enriched in this region including ACTL6A and SMARCA4. This preferential region of linkage between SMARCE1 and cBAF, but not PBAF subunits suggested a structural basis for the cBAF-specific biochemical perturbations that we observed upon SMARCE1 loss.

We next mapped these cross-link sites on to recent cryo-electron microscopy (cryo-EM)-based 3D structures of BAF complexes bound to the nucleosome[2,15,34]. Such structures partially resolved the SMARCE1 subunit and included the BAF CBR (amino acids 172–276), which exhibits a curved, 'U-like' structure within the core module, linking the C terminus of ARID1A (Arm repeat domain) with the SMARCA4 ATPase and members of the initial core module, SMARCC1/2 and SMARCD1/2 (Fig. 2b (upper) and Extended Data Fig. 2a,b). Importantly, integrating CX-MS data, we found that the SMARCE1 N terminus, although not solved in the context of the BAF complex cryo-EM structure, binds near the N-terminal SMARCA4 HSA domain of the ATPase module at its contact point with the ARP module (amino acids 446–480 of SMARCA4) (Fig. 2b (lower) and Extended Data Fig. 2a). These data suggest that the N terminus of SMARCE1, which contains the cBAF-specific interacting region and the HMG DNA-binding domain, extends away from the core and toward the nucleosome.

We next examined cross-links between SMARCE1 and other cBAF subunits in the cBAF-unbound (apo, free) and nucleosome core particle (NCP)-bound configurations. Interestingly, in the NCP-bound configuration, the SMARCE1 N-terminal HLA region (amino acids K146–K166) switches from predominantly tethering the ARID1A C terminus within the core module to predominantly tethering the SMARCA4 ATPase, along its HSA domain, tracking up toward the NCP-ATPase module interaction region (Fig. 2c and Supplementary Table 2). Notably, cross-links between SMARCE1 K166 and the SMARCA4 ATPase increased upon NCP binding, including those links at positions K455 and K458 along the HSA domain of SMARCA4, and positions K303, K371 and K379 of the ACTL6A subunit within the ARP module adjacent to the SMARCA4 HSA (Fig. 2b,c). Sites of decreased cross-linking included K146 of SMARCE1 to ARID1A the core module, indicative of a switch in SMARCE1 subunit interactions upon NCP engagement. These data suggest that the N terminus of SMARCE1 differentially associates with nearby subunits in NCP-bound and -unbound states, and may be rigidified upon NCP binding, probably via its HMG domain binding extra-nucleosomal DNA at the DNA exit site.

We next sought to determine whether this module-linking, 'paperclip'-like subunit was present in yeast, despite the fact that SMARCE1 does not have a homolog based on amino acid conservation alone. We aligned structures of the human cBAF complex (PDB: 6LTJ), yeast SWI/SNF (PDB: 6UXW) and yRSC (PDB: 6KW4) and found that although not conserved by amino acid sequence, the ySWI/SNF Snf6 subunit exhibited high structural similarity to SMARCE1, with a U-like shape linking the Snf2 ATPase and the Swi1 and Swi3 members of the core module[33–36] (Fig. 2d (left)). Snf6 has long been considered a yeast-specific component that was lost through evolution to mammalian complexes[35,37–39]. Further, CX-MS studies performed on ySWI/SNF complexes[40] similarly revealed N-terminal binding to the ARID1A/B paralog, Swi1, and the SMARCA4/2 and ACTL6A/B paralogs, Snf2 and Arp7, respectively (Extended Data Fig. 2e,f). Although not structurally resolved in yRSC, the resolved portion of the Htl1 subunit is positioned differently and hence may be the SMARCE1/Snf6 structural homolog (Extended Data Fig. 2f–h). Collectively, these comparative biophysical and structural analyses highlight a potentially conserved structural role for SMARCE1 and Snf6 in cBAF and ySWI/SNF, respectively, despite highly divergent amino acid sequences.

We next performed restriction enzyme accessibility assays (REAA) and ATPase measurements on endogenous WT and SMARCE1-deficient complexes, purified by SMARCA4 and SS18, members of the ATPase module, as well as ARID1A and ARID2, specific components of cBAF and PBAF complexes, respectively (Fig. 2d). Indeed, BAF complexes purified in the SMARCE1-deficient setting exhibited a statistically significant reduction in both nucleosome remodeling activity and ATP consumption on mononucleosomes in vitro, compared with WT complexes (Fig. 2e,f). Evaluation of residual cBAF compared with PBAF complexes isolated from the nuclear extract of WT and SMARCE1 KO cells showed that PBAF-mediated nucleosome remodeling and

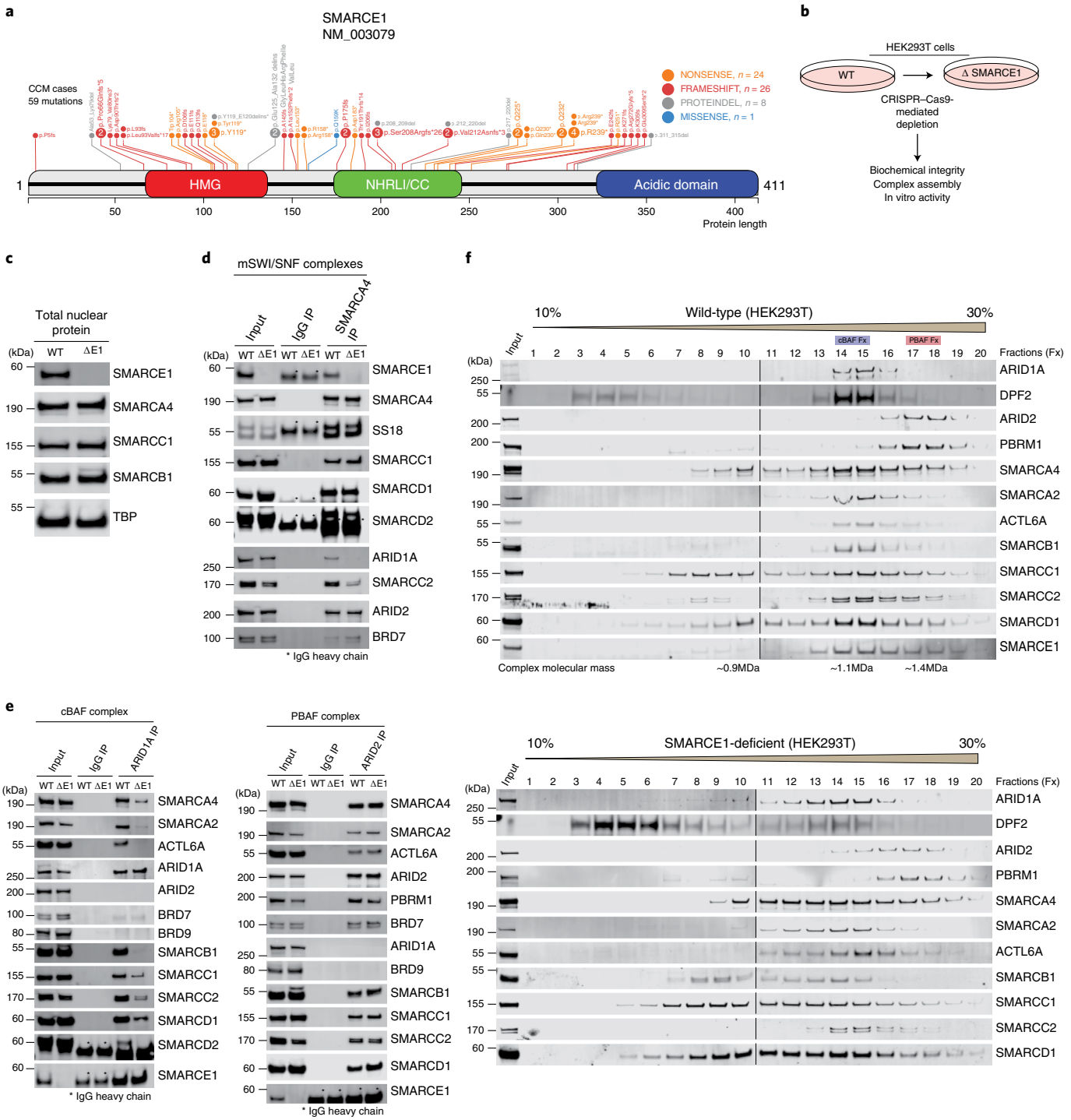

Fig. 1 | SMARCE1 deletion, associated with ~100% of CCM, selectively impacts the stability of cBAF complexes. a, Mutations in *SMARCE1* identified in 59 CCM cases to date, represented as protein-level changes indicated on the SMARCE1 57 kDa protein. **b**, Schematic for the generation of SMARCE1-deficient HEK293T cells using CRISPR–Cas9 and subsequent biochemical experiments. **c**, Immunoblot for selected mSWI/SNF components performed on total nuclear protein, confirming SMARCE1 KO. **d**, IP of the SMARCA4 ATPase in WT and SMARCE1-deficient HEK293T cells, with immunoblot for selected mSWI/SNF subunits. **e**, IP of ARID1A (cBAF-specific; right) and ARID2 (PBAF-specific; left) in WT and SMARCE1-deficient HEK293T cells, with immunoblot for selected mSWI/SNF subunits. **f**, Density sedimentation experiments using 10%–30% glycerol gradients performed on nuclear extracts isolated from WT and SMARCE1-deficient HEK293T cells, with subsequent immunoblotting for mSWI/SNF subunits. Blue and red bars indicate peak sedimentation fractions for cBAF and PBAF complexes, respectively, in WT cells. Representative of $n \geq 3$ experiments with similar results (**c**–**f**).

ATPase activities were either unaffected or modestly affected by SMARCE1 loss (Fig. 2e,f). Taken together, these results highlight the function of SMARCE1 in enabling cBAF-mediated nucleosome remodeling activities.

SMARCE1 loss attenuates cBAF chromatin binding and activity. We next sought to evaluate the impact of SMARCE1 loss on the genome-wide targeting of mSWI/SNF complexes as well as associated DNA accessibility and gene expression. We generated

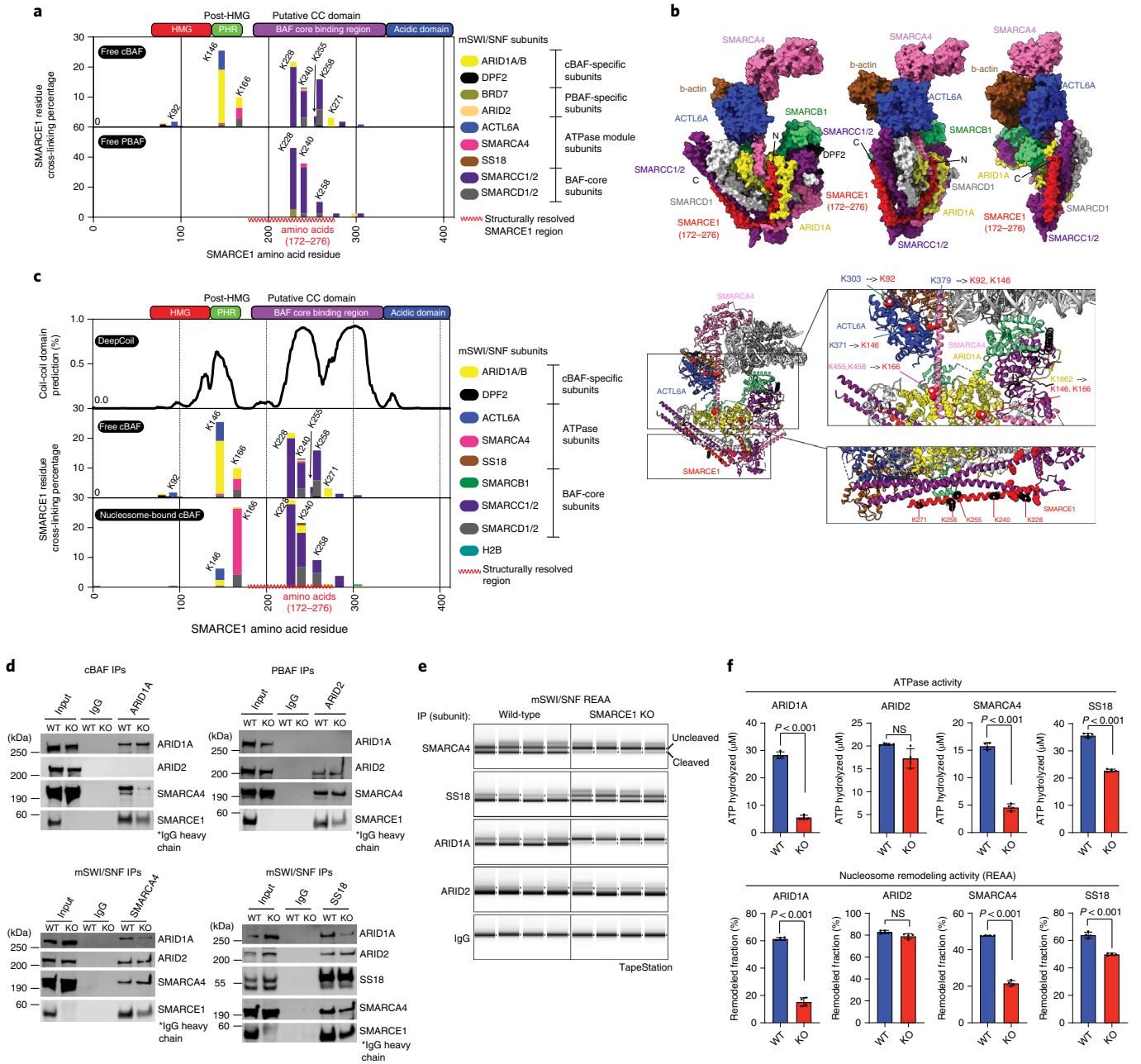

Fig. 2 | SMARCE1 interactions and structural conformation underlie cBAF-specific functions. a, CX-MS analyses performed on purified human cBAF and PBAF complexes, in solution (apo). Cross-links are plotted as a percentage of total SMARCE1 cross-links recovered in the dataset, with the mSWI/SNF subunit to which they tether indicated in the legend. Selected cross-linked lysine (K) residues of SMARCE1 are labeled. SMARCE1 region resolved in human BAF cryo-EM structure is represented by the red zigzag stretch representing amino acids 172–276. Domains are labeled. **b**, (Upper) Integrated 3D structural and CX-MS analyses using cryo-EM structure of the human BAF complex (PDB: 6LTJ). SMARCE1 is highlighted in red with amino acids 172–276 resolved in the structure. (Lower) Key lysine–lysine linkages between mSWI/SNF subunits and SMARCE1 as indicated in **a** for unbound (apo) cBAF. **c**. CX-MS analyses performed on purified human cBAF complexes in nucleosome-unbound and -bound states. Cross-links are plotted as a percentage of total SMARCE1 cross-links recovered in the dataset, and are marked by the mSWI/SNF subunit to which they tether (legend). Selected cross-linked lysine (K) residues of SMARCE1 are labeled. DeepCoil coiled-coil prediction scores are indicated on the top row. **d**, Purification of cBAF (ARID1A) and PBAF (ARID2) complexes in SMARCE1 WT and KO cells used for functional studies; representative of $n = 3$ experiments. **e**, REAA performed on immunoprecipitated complexes in WT and KO conditions, with DNA cleavage measured by TapeStation; representative of $n = 3$ experiments. **f**. Quantification of $n = 4$ experimental replicates for ATPase consumption assays measured by ADP-Glo and remodeling activity, measured by REAA, performed on IP for residual cBAF (ARID1A IP), PBAF (ARID2 IP) and the ATPase module (SMARCA4 and SS18 IPs). Bars represent s.e.m. *P* values derived from the two-sided *t*-test are indicated. NS, not significant.

SMARCE1-deficient arachnoid cells (AC7 cell line; clones AC21 and AC29) isolated from the meninges of a healthy individual[41] using CRISPR–Cas9-mediated editing (Fig. 3a) and performed chromatin immunoprecipitation sequencing (ChIP–seq) for mSWI/SNF subunit proteins and histone modifications. Further, we performed an assay for transposase-accessible chromatin using

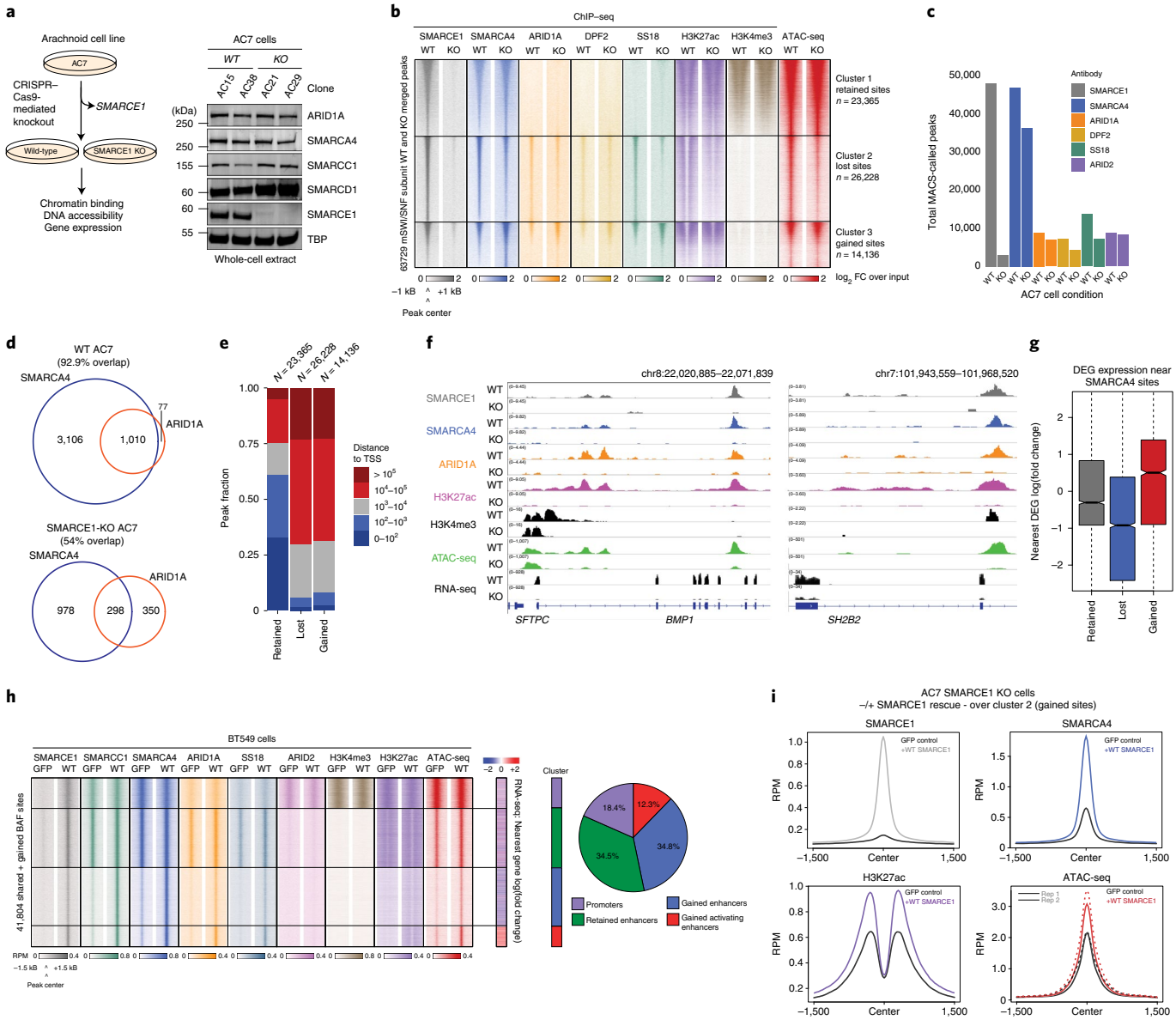

Fig. 3 | SMARCE1 loss reduces cBAF occupancy and DNA accessibility over distal enhancer sites genome-wide. a, Schematic indicating the strategy for generating SMARCE1-deficient AC7 arachnoid cells for genomic interrogation (ChIP–seq/Cut&Tag, ATAC-seq, RNA-seq). **b**, Density heatmaps reflecting chromatin occupancy of SMARCE1, SMARCA4, ARID1A, DPF2, SS18, H3K27ac and H3K4me3, as well as ATAC-seq over all BAF merged peaks in WT and SMARCE1-deficient conditions. **c**, Plot depicting ChIP-seq/Cut&Tag peak numbers in WT and KO cells. **d**, Venn diagrams depicting the overlap between SMARCA4 (ATPase module) and ARID1A (cBAF core module) peaks (TSS-distal) in SMARCE1 WT and KO cells. **e**, Distance to TSS stacked bar graphs for SMARCA4 retained, lost and gained sites in AC7 WT versus SMARCE1-deficient cells. **f**, Example loci reflecting loss in distal enhancer targeting by BAF complexes, resultant accessibility and gene expression at the *BMP1* and *SH2B2* loci. **g**, log(fold change) of differentially expressed genes (DEGs) nearest retained, gained and lost sites. **h**, Heatmap depicting K-means clustering of BT549 ChIP–seq, ATAC-seq and RNA-seq data from naive and SMARCE1 rescue conditions. Pie chart showing distribution of peaks is shown to the right. **i**, Metaplots for SMARCE1, SMARCA4 and H3K27ac ChIP–seq and ATAC-seq in AC7 SMARCE1 KO + green fluorescent protein (GFP) control and +SMARCE1 conditions over gained sites (Cluster 2).

sequencing (ATAC-seq) to evaluate the effect of SMARCE1 loss on genome-wide DNA accessibility (Fig. 3b). Notably, and in line with our biochemical and structural findings, we observed marked attenuation in BAF complex stability as well as H3K27ac on the genome at a cluster of ~26,000 sites (Cluster 2), at which other subunits of the cBAF ATPase module (that is SS18) and the cBAF-specific ARID1A and DPF2 were also reduced (Fig. 3b,c and Extended Data Fig. 3a). Further, co-occupancy of the ATPase (SMARCA4) and the core module (ARID1A) was markedly reduced at transcription start site (TSS)-distal sites of cBAF occupancy in the KO setting (Fig. 3d). By contrast, chromatin occupancy profiling for ARID2, which specifically marks PBAF complexes and is required for the ATPase module to assemble on to the PBAF core[2] did not show changes upon SMARCE1 loss (Fig. 3c and Extended Data Fig. 3a). Sites exhibiting reductions in cBAF complex targeting and associated DNA accessibility were TSS-distal, whereas unchanged (retained) sites were primarily localized to promoters (Fig. 3e). The enhancer-specific loss of genomic targeting and subsequent DNA accessibility was paired with reductions in gene expression, exemplified at the *BMP1* and *SH2B2* loci (Fig. 3f,g and Extended Data Fig. 3b). We also identified a cluster of gained accessibility and residual cBAF complex subunit occupancy (Cluster 3) over which we observed increased

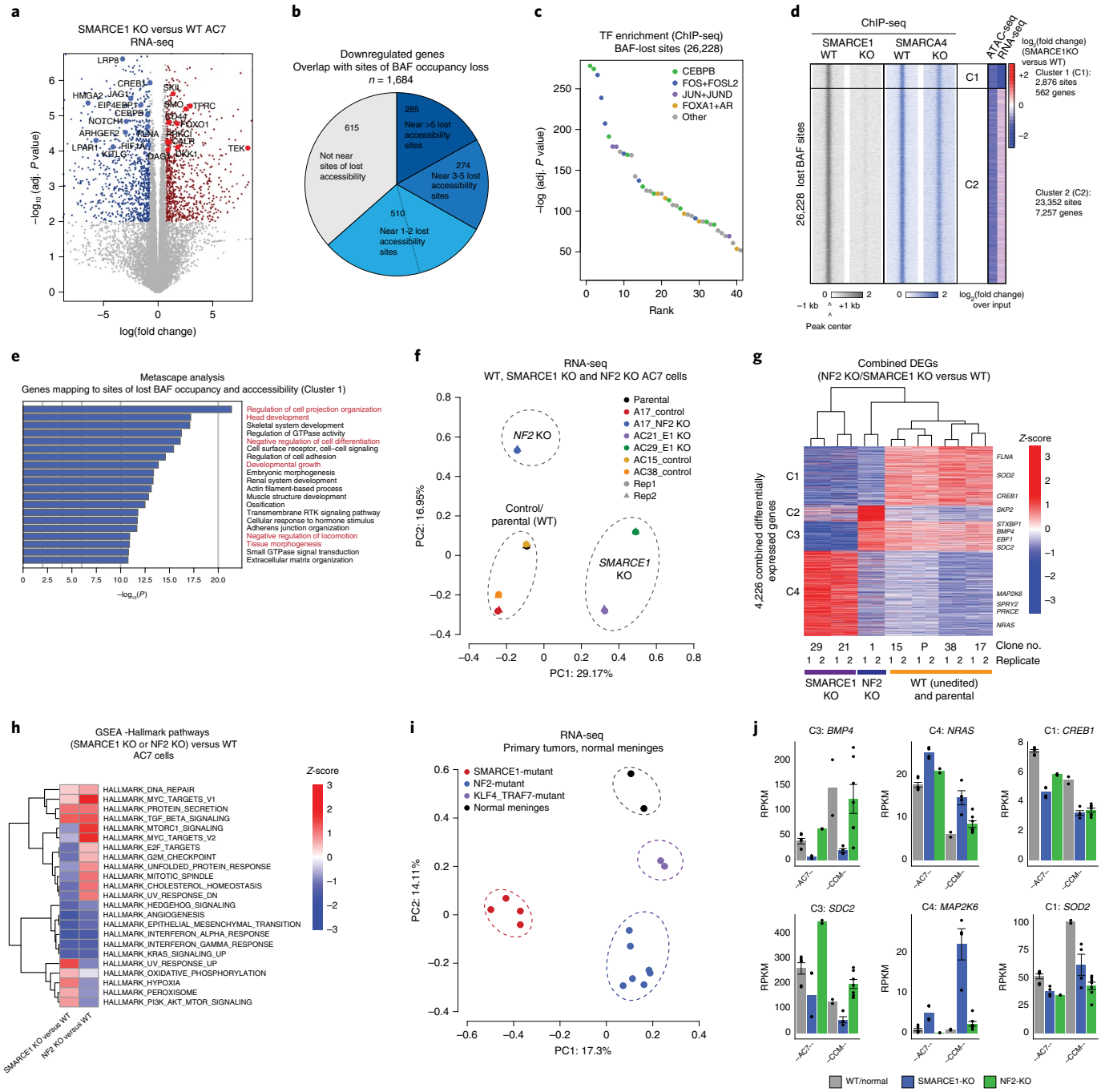

Fig. 4 | SMARCE1 loss alters transcriptome in SMARCE1-deficient AC7 cells and in CCM tumors. a, Volcano plot showing DEGs in SMARCE1-deficient AC7 cells relative to the WT condition. Red and blue dots represent genes significantly upregulated and downregulated, respectively (adj. $P < 0.01$); representative of $n = 3$ experiments. **b**, Pie chart characterizing downregulated DEG expression nearest to sites of BAF occupancy loss. **c**, Transcription factor enrichment analysis within ChIP–seq peak database by LOLA over sites of BAF occupancy loss in SMARCE1-deficient AC7 cells. **d**, Density heatmap displaying SMARCE1 and SMARCA4 occupancy levels at sites of BAF occupancy loss in AC7 cells. $\log_2$(fold change) values of accessibility and nearest gene expression in SMARCE1-deficient cells relative to the WT condition are also displayed. Data were divided into two groups by K-means clustering using the RNA-seq $\log_2$(fold change) values. **e**, Gene ontology analysis by Metascape using 562 genes nearest to Cluster 1 sites in **d**. **f**, PCA analysis on RNA-seq data from control, SMARCE1-deficient and NF2-deficient AC7 cells. **g**, Heatmap of combined DEGs from RNA-seq data in control, SMARCE1 KO and NF2 KO conditions. After Z-score transformation, K-means clustering was used to partition the data into four groups. **h**, GSEA results show differential gene set enrichment (using Hallmark MSIGDB gene set collection) between SMARCE1- and NF2-deficient AC7 cells. **i**, PCA analysis on RNA-seq data from CCM SMARCE1-deficient, NF2-deficient and KLF/TRAF7-deficient tumors. **j**, Bar plots displaying gene expression for select genes (*BMP4*, *NRAS*, *CREB1*, *SDC2*, *MAP2K6* and *SOD2*) in WT, SMARCE1-deficient and NF2-deficient AC7 cells and primary CCM tumors. Mean with error bars representing s.d. are shown for primary tumors, derived from $n \geq 3$ biological replicates (samples).

binding of non-ATPase-bound residual core module subunits (that is ARID1A and DPF2) in the SMARCE1 KO condition over open DNA-accessible sites (Fig. 3b,c and Extended Data Fig. 3a). To complement these findings, we rescued SMARCE1 (or a green fluorescent protein control) into SMARCE1-deficient BT549 cells (Extended Data Fig. 3c,d). Again here, SMARCE1 rescue resulted in substantial de novo targeting of cBAF (but not PBAF) complexes as well as accessibility generation, with genes nearest gained peaks substantially upregulated (Fig. 3h,i and Extended Data Fig. 3f–j). This was further confirmed in SMARCE1 KO AC7 cells rescued with SMARCE1 (Extended Data Fig. 3k,l). These data indicate that disruptions in cBAF targeting mediated by SMARCE1 loss result in loss of DNA accessibility and target gene expression.

SMARCE1 loss generates distinct gene regulatory programs. SMARCE1 deletion resulted in 1,684 genes significantly downregulated and 1,772 genes significantly upregulated (Fig. 4a and Extended Data Fig. 4a), and we identified a subset of 1,069 downregulated genes (63% of all 1,684 downregulated differentially expressed genes (DEGs)) mapping to sites at which BAF complex occupancy was reduced in the SMARCE1 KO condition (near at least one lost site; interquartile range (IQR) = −2.11 to −0.48; $P < 0.01$) (Fig. 4b). Motif analyses performed using HOMER and LOLA over BAF-lost sites revealed enrichment of JUN, FRA, CEBPB, NF1 and NF1-FOXA1 motifs, consistent with defects in cBAF-mediated DNA accessibility over critical transcription factor binding sites known to have roles in arachnoid and meningeal cell function and cell division[42] (Fig. 4c and Extended Data Fig. 4b, left). Further, rescue of SMARCE1 into SMARCE1 KO AC7 cells returned the same collections of motifs (Extended Data Fig. 4b, right). We identified a subcluster of genes ($n = 562$; near 10%–15% of all sites) that were most significantly downregulated and for which nearby BAF complex occupancy and DNA accessibility were strongly reduced (associated with an average of approximately five lost (putative enhancer sites; IQR = −4.67 to −2.44) (Fig. 4d and Extended Data Fig. 4c). Examples included *RSG4*, *LPAR1* and *TRPC6* genes (Extended Data Fig. 4c). Metascape analyses revealed enrichment of extracellular matrix organization, developmental growth, sensory organ development and tissue morphogenesis pathways, consistent with the oncogenic function of SMARCE1 loss in CCM (Fig. 4e).

Given that meningiomas are often driven by loss of the *NF2* tumor suppressor gene, we next sought to compare the gene expression profiles of SMARCE1 KO and NF2 KO AC7 cells (Extended Data Fig. 4d,e). Principal component analysis (PCA) performed on gene expression (RNA sequencing (RNA-seq)) clustered SMARCE1- and NF2-deficient cell types distinctly on PC1 and PC2, respectively, relative to control (WT) cells (Fig. 4f and Extended Data Fig. 4d,e). Unsupervised hierarchical clustering analyses across WT, SMARCE1-deficient or NF2-deficient AC7 cells revealed uniquely up- and downregulated sets of genes, including those that were specific to each KO (SMARCE1 and NF2) and those shared between the conditions (Fig. 4g and Extended Data Fig. 4f–i). For example, we identified that *BMP4*, *EBF1* and *SDC2* were selectively downregulated in the SMARCE1 KO condition, whereas *NRAS* and *MAP2K6* and *SPRY2* were strongly upregulated in SMARCE1 KO condition relative to NF2 KO and WT settings (Fig. 4g and Extended Data Fig. 4g,h). We also identified genes and pathways downregulated in both SMARCE1- and NF2 KO settings (relative to WT), such as *SOD2*, *CREB1* and *FLNA*, suggesting convergent gene regulatory changes, such as in the epithelial-to-mesenchymal transition and interferon responses as well as the mammalian target of rapamycin complex (mTORC) pathway, consistent with studies suggesting the efficacy of mTORC inhibitors in NF2-mutant meningiomas[41] (Fig. 4g,h and Extended Data Fig. 4i).

Finally, we investigated the transcriptional profile of primary meningiomas, including SMARCE1-deficient CCM, NF2-deficient meningiomas and *KLF4*/*TRAF7*-mutated meningiomas, as well as normal meninges from healthy donors as controls. We isolated RNA from four SMARCE1-null tumors, seven NF2-null tumors, two *KLF4*/*TRAF7*-mutated tumors and two normal meninges (Supplementary Table 3). Notably, PCA showed clear segregation of NF2-null, *KLF4*/*TRAF7*-mutated and SMARCE1-null tumors relative to normal meninges (Fig. 4i). Using clustering analyses, we identified gene sets uniquely upregulated and downregulated in SMARCE1- or NF2-loss samples, and in both conditions (Extended Data Fig. 4j–l). For example, SMARCE1-deficient tumors selectively downregulated genes associated with insulin signaling, adipogenesis and WNT signaling, whereas tumors containing either SMARCE1 or NF2 loss downregulated ascular Endothelial Growth Factor A and NO/cGMP pathways (Extended Data Fig. 4j–l). Importantly, we identified several gene expression changes mirrored in primary tumors, such as *MAP2K6* and *NRAS* upregulation in SMARCE1 KO cells and primary CCM, *SDC2* upregulation in *NF2*-mutant meningioma, and *SOD2* and *CREB1* downregulation in both tumor types (Fig. 4j and Extended Data Fig. 4m,n). Taken together, these results indicate the distinct (and shared) gene regulatory consequences of SMARCE1 loss.

SMARCE1 loss results in gained ncBAF genomic targeting. In addition to the large number of genome-wide BAF complex peaks that were lost upon SMARCE1 deletion (Fig. 3), we also identified several SMARCA4-gained peaks (Fig. 5a), a large percentage of which (70%) did not overlap with sites of SMARCE1-bound BAF complex occupancy in the WT setting, indicating the presence of complexes lacking this subunit (Fig. 5a). Over these sites, we characterized the chromatin occupancy of several other mSWI/SNF subunits and histone modifications and found that BRD9, an ncBAF-specific subunit, along with SMARCD1 (which is the only SMARCD paralog that incorporates into ncBAF and functionally clusters with ncBAF[43]) predominantly exhibited gains in occupancy with minimal losses following SMARCE1 deletion (Fig. 5b,c and Extended Data Fig. 5a). Intriguingly, examination

Fig. 5 | SMARCE1 loss increases ncBAF occupancy and DNA accessibility over enhancer sites genome-wide. a, Venn diagram of SMARCE1 and SMARCA4 peaks in both WT and SMARCE1-deficient conditions reflecting genome-wide changes in BAF localization upon SMARCE1 loss in AC7 cells. **b**, Bar plot showing peak numbers for ncBAF complex subunits for both WT and SMARCE1-deficient conditions in AC7 cells. **c**. Density heatmaps reflecting chromatin occupancy of SMARCE1, SMARCA4, SS18, BRD9, H3K27ac and H3K4me3, as well as ATAC-seq in WT and SMARCE1-deficient conditions over gained sites from Cluster 3 in Fig. 3b. **d**, ECDF plots of SMARCA4 $\log_2$(fold change) (relative to WT) as a function of motif count for 286 nonredundant transcription factor archetypes motifs is shown for both AC7 and BT549 over merged BAF peaks. **e**, Motif analysis results by ChromVAR on ATAC-seq data for both AC7 and BT549 cells over merged ATAC-seq peaks. **f**, Density heatmaps reflecting chromatin occupancy of SMARCD1 and BRD9 in WT and SMARCE1-deficient conditions over merged WT and KO SMARCD1 peaks. **g**, Box plots of $\log_2$(fold change) values for DEGs nearest to SMARCD1 peaks in clusters 1, 2 and 3 from **f**. **h**, Gene ontology analysis by Metascape using upregulated DEGs nearest to Cluster 2 sites in **f**. **i**, Pie chart characterizing upregulated DEG expression nearest to sites of ncBAF occupancy gain for Cluster 2 in **f**. **j**, Venn diagram reflecting overlap among sites with SMARCA4 gain, along with accessibility gain by ATAC-seq, and sites nearest to genes with significant increases in expression in SMARCE1-deficient AC7 relative to WT (from Cluster 3 of Fig. 3b). **k**, Lollipop plot displaying expression of select 40 genes upregulated in AC7 cells that are near sites with increases in both BAF binding and accessibility. **l**, Example reflecting gains in enhancer targeting by ncBAF complexes, resultant accessibility and gene expression at the *ITIH5* locus.

of sites gained upon SMARCE1 loss, or conversely, sites lost upon SMARCE1 rescue in BT549 cells and AC7-SMARCE1 KO cells, revealed strong enrichment of CTCF motifs, consistent with previous studies that have indicated localization of ncBAF complexes over CTCF sites[3,44,45] (Fig. 5d,e and Extended Data Fig. 5b). The strong enrichment of CTCF at BAF-bound and accessible sites in the SMARCE1 KO condition suggested increased ncBAF complex targeting as well as nucleosome remodeling activities over these sites (Fig. 5d,e). Examination of all BRD9/SMARCD1-gained peaks (Fig. 5f) indicated promoter-proximal distribution over CTCF and TEAD motifs (Extended Data Fig. 5c–e), again consistent with previous findings by our group and others indicating that ncBAF complex localization is more promoter-proximal than that of cBAF complexes[3,44]. Taken together, these data suggest that gained ncBAF genomic binding occurs in a manner proportional to cBAF complex disruption.

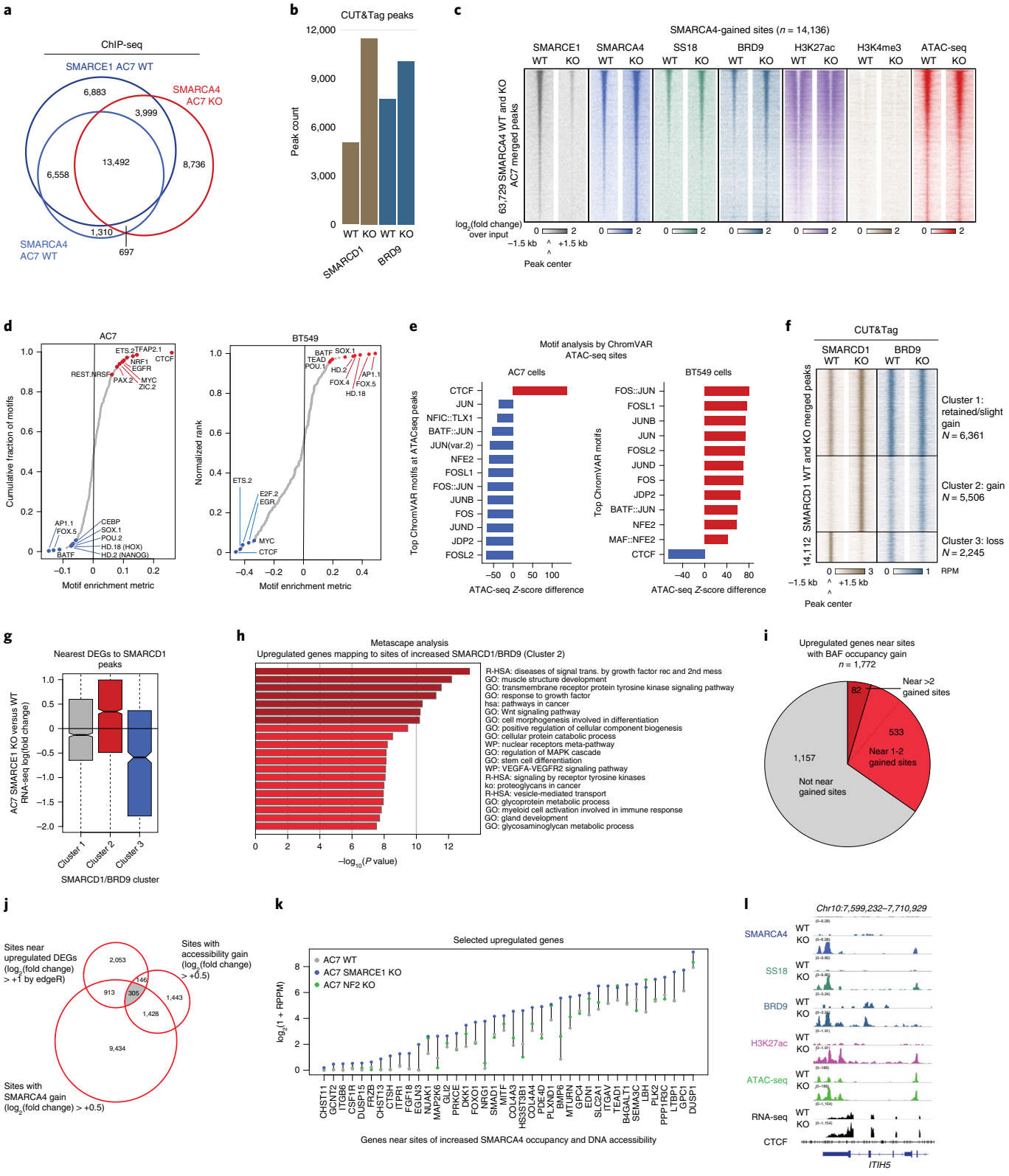

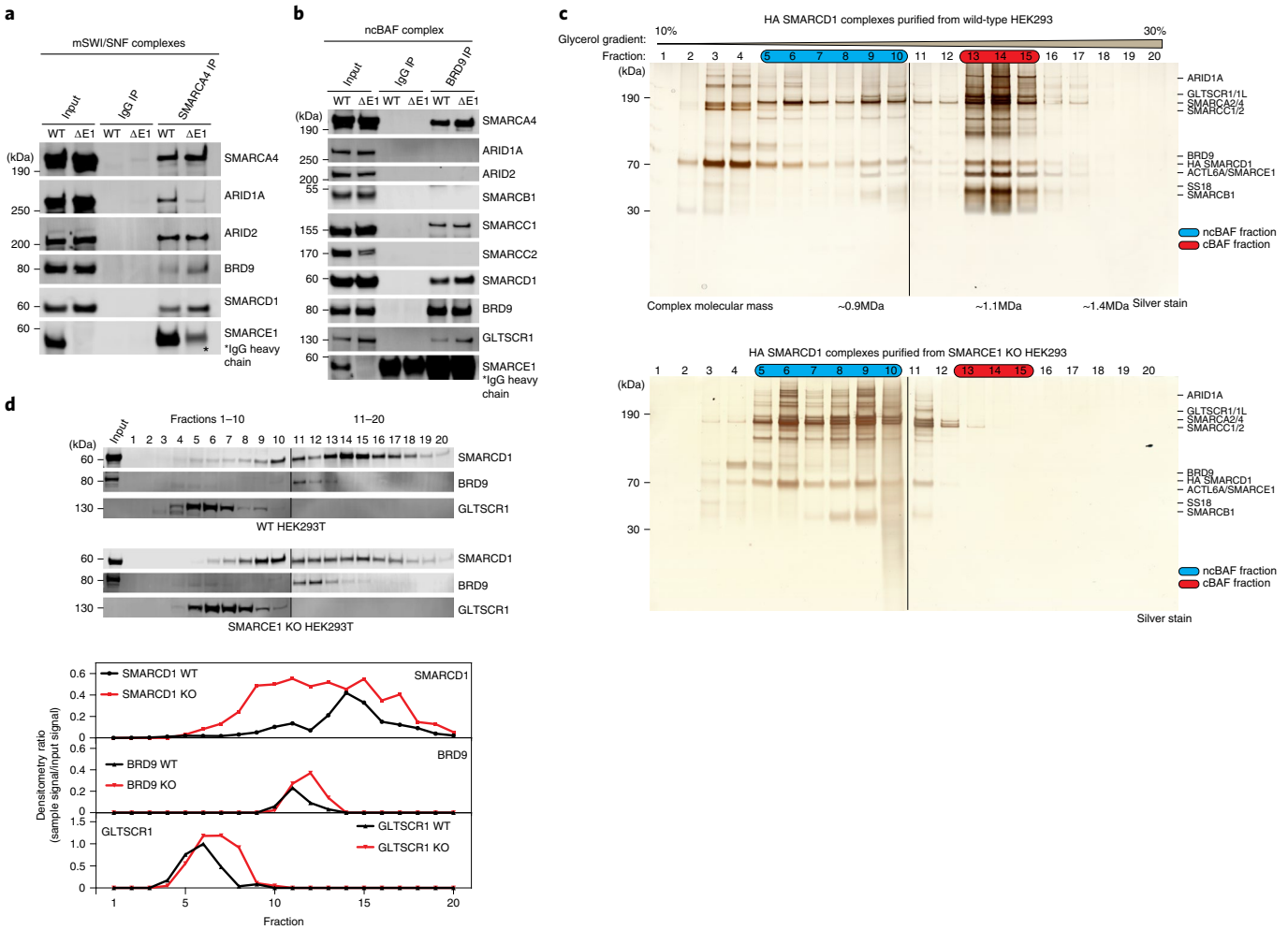

Fig. 6 | SMARCE1 loss results in increased biochemical nucleation of ncBAF complexes. a, IP of SMARCA4 in WT and SMARCE1-deficient HEK293T cells, with immunoblot for selected mSWI/SNF subunits. **b**, IP of BRD9 in WT and SMARCE1-deficient HEK293T cells, with immunoblot for selected mSWI/SNF subunits. **c**, Silver stain performed on density sedimentation (10%–30% glycerol gradient) of HA-SMARCD1-purified mSWI/SNF complexes (capturing all three subtypes) purified from WT and SMARCE1-deficient HEK293T cells. The asterisk denotes HA-SMARCD1 bait. cBAF and ncBAF fractions are indicated and subunits are labeled. **d**, (Upper) Density sedimentation (10%–30% glycerol gradient) followed by ncBAF-specific immunoblotting performed on WT and SMARCE1-deficient HEK293T nuclear extracts. (Lower) Quantitative densitometry performed on SMARCD1, BRD9 and GLTSCR1 levels from immunoblots. Representative of $n = 3$ experiments with similar results (**a**–**d**).

Importantly, these SMARCE1-loss-mediated ncBAF-gained sites (Cluster 2, Fig. 5f) corresponded to increased expression of the nearest genes (Fig. 5g). Gene sets nearest gained ncBAF peaks in SMARCE1-deficient AC7 cells include response to growth factors, tyrosine kinase pathways, WNT signaling and others, suggesting a role for the ncBAF chromatin remodeler in the maintenance of a range of oncogenic programs (Fig. 5h). Further, >33% of significantly upregulated genes mapped to sites of both increased ncBAF complex occupancy and accessibility included genes involved in cell signaling (that is *NRG1*), development and transforming growth factor beta signaling (*BMP6*), among others (Fig. 5i–k). As examples, we observed increased ncBAF peak occupancy at the *ITIH5* and *MS4A7* loci, at which we also observed increased DNA accessibility and gene expression (Fig. 5l and Extended Data Fig. 5f). These studies demonstrate the gained occupancy of ncBAF complexes on chromatin mediated by SMARCE1 deletion, specifically at CTCF and TEAD sites, and implicate their role in gene expression maintenance in CCM.

SMARCE1 loss yields increased ncBAF biochemical abundance. To understand the basis for the increased ncBAF chromatin occupancy and gene regulation genome-wide, a result initially unexpected given that ncBAF complexes do not contain SMARCE1, we next performed biochemical studies to probe the total nuclear protein and SMARCA4-associated abundance of ncBAF complex components. Intriguingly, IP–immunoblot studies performed in SMARCE1 WT and KO conditions in HEK293T cells revealed that although ARID1A was almost entirely absent from SMARCA4-bound complexes, capture of BRD9 and SMARCD1 subunits was substantially increased (Fig. 6a). Further, IP of ncBAF complexes (anti-BRD9) revealed substantially increased pull-down of the SMARCA4 ATPase, as well as ncBAF components, SMARCD1 and GLTSCR1 (Fig. 6b). Density sedimentation studies performed on SMARCD1-bound complexes purified from HEK293T WT and SMARCE1 KO cell types revealed a clear shift in SMARCD1-associated mSWI/SNF complexes to lower molecular mass fractions in the SMARCE1 KO condition, associated with increased assembly of the smaller (~0.87 kDa, ten-subunit) ncBAF complexes (Fig. 6c). In parallel, density sedimentation experiments performed on total nuclear extracts derived from WT and SMARCE1 KO HEK293T cells (Fig. 1b,c) revealed a marked shift in SMARCD1 toward the lower molecular mass fractions in the

SMARCE1 KO condition as well as increased BRD9 and GLTSCR1 protein-level abundance in the ncBAF fractions (Fig. 6d). These studies implicate a protein complex assembly basis for the increased ncBAF abundance, chromatin binding and activity genome-wide in SMARCE1-deficient CCM.

mSWI/SNF inhibition selectively affects SMARCE1-deficient cells. Finally, given the increase in ncBAF assembly and chromatin occupancy paired with concomitant loss of stable cBAF complexes in SMARCE1-deficient cells, we sought to determine whether ncBAF complexes and residual mSWI/SNF complex ATPase activity were required for the maintenance of SMARCE1-deficient AC7 cells. We subjected AC7 WT and KO arachnoid cells to treatment with two distinct small-molecule inhibitors: a degrader of the ncBAF-specific BRD9 component, dBRD9A[3,46–48]; and a recently described dual SMARCA4/SMARCA2 ATPase inhibitor (referred to here as Compound 12 (CMP12))[48] (Fig. 7a).

Treatment of AC7 cells with dBRD9A resulted in near-complete (>95%) degradation of BRD9 in both WT and SMARCE1 KO settings (Fig. 7b). Importantly, we found selective inhibition of cell growth in SMARCE1 KO cells following 5–7 d of treatment (Fig. 7c). dBRD9A treatment affected nearly double the number of changed accessibility sites in SMARCE1 KO compared with WT cells (Fig. 7d), underscoring the enhanced impact of ncBAF in this setting. Sites decreased in accessibility were found at both promoters and enhancers (Extended Data Fig. 6a), and corresponded to CTCF and TEAD motifs, consistent with ncBAF localization (Extended Data Fig. 6b). Further, treatment with dBRD9A resulted in an increased number of significantly downregulated genes in the SMARCE1 KO setting (relative to WT AC7 cells), again indicating the enhanced gene regulatory role for ncBAF complexes in this cBAF-perturbed setting (Fig. 7e). Genes nearest these sites with reduced accessibility following dBRD9A treatment in SMARCE1 KO cells were particularly enriched in beta-integrin signaling, TGF-beta receptor signaling, and MAPK signaling, consistent with a role for ncBAF complexes in proliferative maintenance, cell proliferation and invasion (Fig. 7f). Over 50% of the downregulated genes localized near sites of decreased accessibility upon dBRD9A treatment, 42% (356/859) of which were selectively affected by dBRD9A in the KO condition (not in the WT condition) including *NRG1*, *DLX2* and *ID2* (Fig. 7g).

In parallel, we treated AC7 WT and SMARCE1 KO cells with the SMARCA4/2 dual ATPase inhibitor (CMP12) and indeed, SMARCE1 KO cells exhibited enhanced sensitivity to compound exposure (Fig. 7h and Extended Data Fig. 6c). Proliferative attenuation was specific to the SMARCE1-deficient setting, as NF2 KO and all other AC7 clones were significantly less sensitive (Extended Data Fig. 6c,d). Notably, we observed far fewer accessibility changes in the SMARCE1 KO setting relative to in WT cells, consistent with the fact that cBAF complexes, which are the complexes with the most nuclear abundance and main generators of ATPase activity, are significantly compromised upon SMARCE1 deletion (Fig. 7i and Extended Data Fig. 6e). However, in comparing WT and KO cells, roughly equal numbers of genes were down- and up-regulated (Extended Data Fig. 6e–g). Gene processes downregulated in SMARCE1 KO cells upon CMP12 treatment, in a dose-dependent manner, enriched for TGF-beta, beta-integrin, AP1 signaling and syndecan signaling, many of which mirrored top pathways impacted by dBRD9A (Fig. 7j and Extended Data Fig. 6h–l). Coupled with the fact that processes affected by both dBRD9A and CMP12 in the WT cells were markedly different from those impacted in SMARCE1 KO cells, these data indicate the impact of CMP12 on the catalytic activity of ncBAF complexes. Collectively, these data highlight the enhanced impact of ncBAF disruption in SMARCE1-deficient cells and suggest potential therapeutic utility of ncBAF-modulating agents.

We next combined these two datasets (dBRD9A and CMP12) to determine the genomic sites and genes that are dependent on both ncBAF targeting (via BRD9) and ncBAF ATPase activity (via the ATPase module) (Fig. 7k). Genes downregulated by both small molecules included those enriched in cell cycle related, extracellular matrix, structure pathways (Fig. 7f,j,k and Extended Data Fig. 6m), and genes upregulated corresponded to apoptosis, negative regulators of signal transduction and actin cytoskeleton organization (Extended Data Fig. 6n). Further, within the genes that were altered in expression by both dBRD9A and CMP12 in the KO condition only (not affected in the AC7 WT cells), we identified a subset of genes for which changes in expression were reversed by both treatments selectively in the SMARCE1 KO (cBAF) perturbation setting, such as *NRG1*, *MEF2C* and *FGF9* (downregulated) and *ELK1*, *EPHA2* and *BCL2L1* (upregulated), underscoring the ncBAF-mediated control (and the requirement for its ATPase activity) of these processes and genes (Fig. 7l and Extended Data Fig. 6o).

Finally, we integrated these data with primary CCM RNA-seq to identify genes whose expression was strongly upregulated in both SMARCE1-deficient AC7 cells and CCM primary tumor specimens, and whose expression was attenuated upon treatment with both dBRD9A and CMP12 (Fig. 7m). These genes included *COL28A1*, *FGF9*, *CSF1R*, and *PTK7*, among others all known to promote cancer cell proliferation, migration and invasion. Taken together, we identify altered gene regulatory programs central to CCM that are

Fig. 7 | Small-molecule inhibition of ncBAF complexes attenuates oncogenic gene expression and proliferation of SMARCE1-deficient cells. **a**, Schematic depicting treatment of AC7 cells with dimethylsulfoxide (DMSO), dBRD9A (BRD9 degradation) or CMP12 (BAF ATPase inhibition). **b**, Immunoblot for selected mSWI/SNF components performed on total nuclear protein of AC7 cells treated with dimethylsulfoxide, dBRD9A or CMP12. **c**, Time-course graph depicting WT and SMARCE1 KO cell viability following dBRD9A treatment (2 or 10 μM). Error bars represent the s.d. of the mean. *P* values derived from two-sided *t*-test are indicated and are calculated from $n = 3$ biologically independent replicate experiments. **d**,**e**, Stacked bar plots displaying numbers of differentially (**d**) accessible sites or (**e**) genes after dBRD9A treatment in WT and SMARCE1 KO AC7 cells. DN, downregulated; UP, upregulated. **f**, MSigDB pathway terms by GREAT analysis performed on dBRD9A-mediated differentially accessible sites in SMARCE1 KO AC7 cells. IFN-γ, interferon-gamma; PIP2, phosphatidylinositol 4,5-bisphosphate. **g**, Volcano plot reflecting DEGs in SMARCE1 KO AC7 cells after dBRD9A treatment relative to dimethylsulfoxide. Blue dots represent genes with significantly downregulated DEGs (adj. $P < 0.01$) and purple dots represent genes that are downregulated and overlapping with sites losing accessibility upon dBRD9A treatment. The adjacent pie chart characterizes the distribution of downregulated genes in the SMARCE1 KO cells after dBRD9A treatment. **h**, Time course of CMP12 treatment of WT and SMARCE1 KO AC7 cells over 5 d at 50 nM CMP12. Error bars indicate s.d. with center representing the mean value. *P* values derived from a two-sided *t*-test are indicated and calculated from $n = 3$ biologically independent replicate experiments. NS, not significant. **i**, Stacked bar plots displaying numbers of differentially accessible sites after CMP12 treatment in WT and SMARCE1 KO AC7 cells. **j**, GREAT analysis performed on differentially accessible sites after CMP12 treatment in SMARCE1-deficient AC7 cells. **k**, Venn diagrams highlighting upregulated and downregulated DEGs after dBRD9A and CMP12 treatment specifically in SMARCE1-deficient cells. **l**, Unsupervised hierarchical clustering of the $\log_2$(fold change) values for 40 selected genes derived from the intersections of the Venn diagrams in **k**. **m**, Heatmaps reflecting selected genes upregulated in primary CCM tumors (relative to normal meninges) that are also upregulated in SMARCE1 KO AC7 cells (relative to WT AC7) and are affected by both dBRD9A and CMP12 treatment.

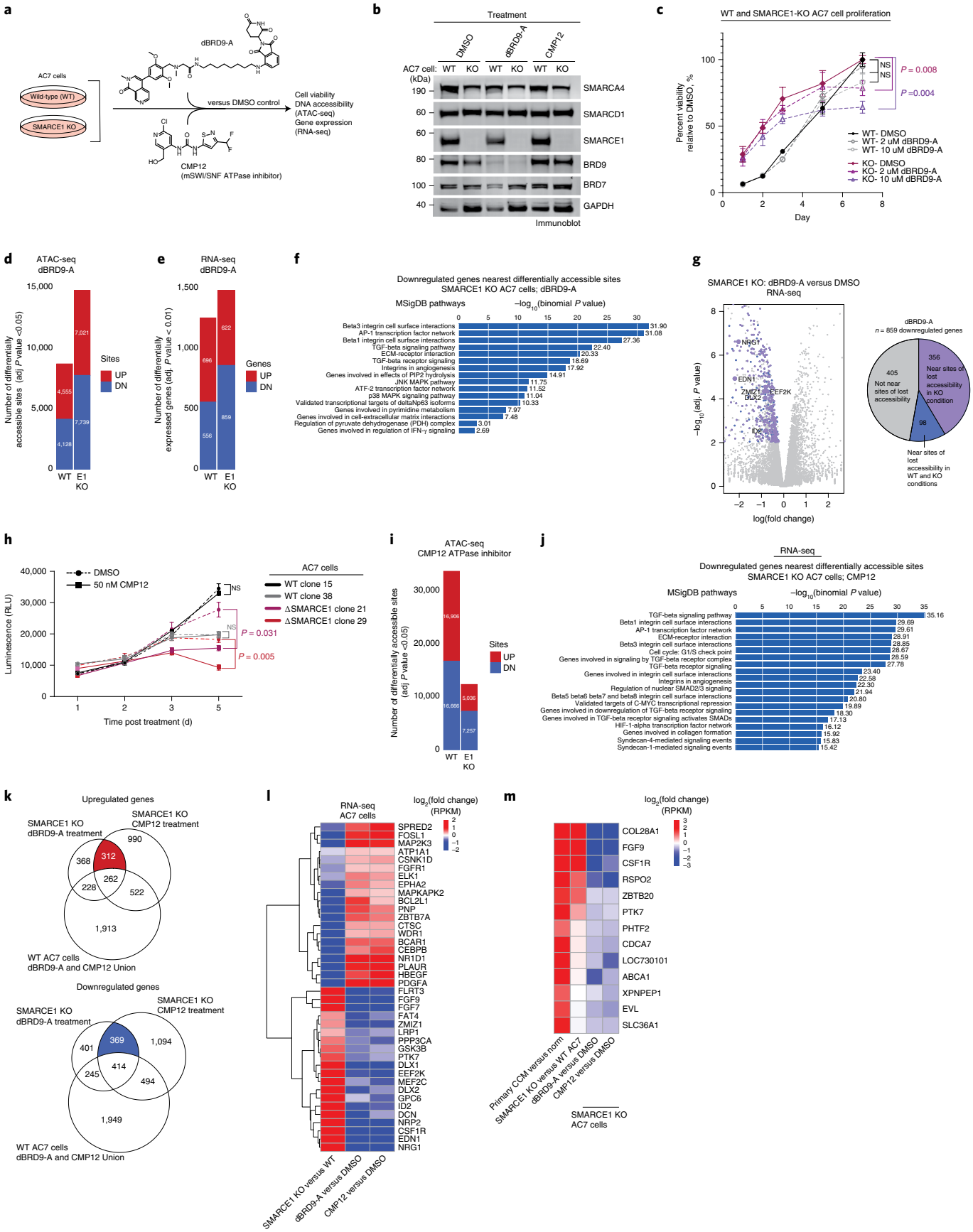
a
dBRD9-A
AC7 cells
Wild-type (WT)
SMARCE1 KO
versus DMSO control
Cell viability
DNA accessibility
(ATAC-seq)
Gene expression
(RNA-seq)
CMP12
(mSWI/SNF ATPase inhibitor)
b
Treatment
DMSO
dBRD9-A
CMP12
AC7 cell: WT KO WT KO WT KO
(kDa)
190
60
60
80
100
40
SMARCA4
SMARCD1
SMARCE1
BRD9
BRD7
GAPDH
Immunoblot
c
WT and SMARCE1-KO AC7 cell proliferation
Percent viability relative to DMSO, %
Day
NS
NS
P = 0.008
P =0.004
WT- DMSO
WT- 2 uM dBRD9-A
WT- 10 uM dBRD9-A
KO- DMSO
KO- 2 uM dBRD9-A
KO- 10 uM dBRD9-A
d
ATAC-seq
dBRD9-A
Number of differentially accessible sites (adj P value <0.05)
Sites
UP
DN
WT
E1
KO
e
RNA-seq
dBRD9-A
Number of differentially expressed genes (adj. P value < 0.01)
Genes
f
Downregulated genes nearest differentially accessible sites
SMARCE1 KO AC7 cells; dBRD9-A
MSigDB pathways
−log10(binomial P value)
Beta3 integrin cell surface interactions 31.90
AP-1 transcription factor network 31.08
Beta1 integrin cell surface interactions 27.36
TGF-beta signaling pathway 22.40
ECM-receptor interaction 20.33
TGF-beta receptor signaling 18.69
Integrins in angiogenesis 17.92
Genes involved in effects of PIP2 hydrolysis 14.91
JNK MAPK pathway 11.75
ATF-2 transcription factor network 11.52
p38 MAPK signaling pathway 11.04
Validated transcriptional targets of deltaNp63 isoforms 10.33
Genes involved in pyrimidine metabolism 7.97
Genes involved in cell-extracellular matrix interactions 7.48
Regulation of pyruvate dehydrogenase (PDH) complex 3.01
Genes involved in regulation of IFN-γ signaling 2.69
g
SMARCE1 KO: dBRD9-A versus DMSO
RNA-seq
−log10(adj. P value)
log(fold change)
NRG1
EDN1
ZMIZ1
EEF2K
DLX2
ID2
dBRD9-A
n = 859 downregulated genes
356
Near sites of lost accessibility in KO condition
405
Not near sites of lost accessibility
98
Near sites of lost accessibility in WT and KO conditions
h
Luminescence (RLU)
Time post treatment (d)
DMSO
50 nM CMP12
NS
NS
P = 0.031
P = 0.005
AC7 cells
WT clone 15
WT clone 38
ΔSMARCE1 clone 21
ΔSMARCE1 clone 29
i
ATAC-seq
CMP12 ATPase inhibitor
Number of differentially accessible sites (adj. P value <0.05)
Sites
UP
DN
WT
E1
KO
j
RNA-seq
Downregulated genes nearest differentially accessible sites
SMARCE1 KO AC7 cells; CMP12
MSigDB pathways
−log10(binomial P value)
TGF-beta signaling pathway 35.16
Beta1 integrin cell surface interactions 29.69
AP-1 transcription factor network 29.61
ECM-receptor interaction 28.91
Beta3 integrin cell surface interactions 28.85
Cell cycle: G1/S check point 28.67
Genes involved in signaling by TGF-beta receptor complex 28.59
TGF-beta receptor signaling 27.78
Genes involved in integrin cell surface interactions 23.40
Integrins in angiogenesis 22.58
Regulation of nuclear SMAD2/3 signaling 22.30
Beta5 beta6 beta7 and beta8 integrin cell surface interactions 21.34
Validated targets of C-MYC transcriptional repression 20.80
Genes involved in downregulation of TGF-beta receptor signaling 19.89
Genes involved in TGF-beta receptor signaling activates SMADs 18.30
HIF-1-alpha transcription factor network 17.13
Genes involved in collagen formation 16.12
Syndecan-4-mediated signaling events 15.92
Syndecan-1-mediated signaling events 15.83
15.42
k
Upregulated genes
SMARCE1 KO dBRD9-A treatment
SMARCE1 KO CMP12 treatment
WT AC7 cells dBRD9-A and CMP12 Union
Downregulated genes
SMARCE1 KO dBRD9-A treatment
SMARCE1 KO CMP12 treatment
WT AC7 cells dBRD9-A and CMP12 Union
l
RNA-seq
AC7 cells
log2(fold change) (RPKM)
SPRED2
FOSL1
MAP2K3
ATP1A1
CSNK1D
FGFR1
ELK1
EPHA2
MAPKAPK2
BCL2L1
PNP
ZBTB7A
CTSC
WDR1
BCAR1
CEBPB
NR1D1
PLAUR
HBEGF
PDGFA
FLRT3
FGF9
FGF7
FAT4
ZMIZ1
LRP1
PPP3CA
GSK3B
PTK7
DLX1
EEF2K
MEF2C
DLX2
GPC6
ID2
DCN
NRP2
CSF1R
EDN1
NRG1
SMARCE1 KO versus WT
dBRD9-A versus DMSO
CMP12 versus DMSO
m
log2(fold change) (RPKM)
COL28A1
FGF9
CSF1R
RSPO2
ZBTB20
PTK7
PHTF2
CDCA7
LOC730101
ABCA1
XPNPEP1
EVL
SLC36A1
Primary CCM versus norm
SMARCE1 KO versus WT AC7
dBRD9-A versus DMSO
CMP12 versus DMSO
SMARCE1 KO AC7 cells

mediated by increased abundance and activity of ncBAF complexes, highlighting a potential therapeutic strategy for CCM mediated by cBAF complex impairment.

Discussion

Here we define a unique biochemical role for SMARCE1 in linking together the ATPase and core modules of the cBAF complex, thus enabling cBAF formation and nucleosome remodeling activities. Importantly, protein-level compromise in the cBAF assembly pathway results in increased biochemical assembly, genome-wide chromatin-associated abundance and function of ncBAF complexes. This unique SWI/SNF deficiency hallmark to CCM tumors generates the CCM gene expression signature found in primary tumors and renders SMARCE1-deficient cells uniquely sensitive to small-molecule-mediated disruption of ncBAF catalytic and targeting activities, implicating potential therapeutic opportunities for this aggressive cancer type.

Our results point to SMARCE1 as a key lynchpin of the cBAF, but not PBAF, complex, despite being a stable subunit of both complexes. SMARCE1 tethers together the core and ATPase modules and its absence results in cBAF-specific destabilization, both biochemically and on the genome (Figs. 1–3). Intriguingly, Snf6, a member of the yeast SWI/SNF complex, exists as a structural homolog for SMARCE1, suggesting an evolutionarily conserved function for the subunit that could not be appreciated by conventional sequence conservation analyses (Fig. 2 and Extended Data Fig. 2). A potential SMARCE1 structural homolog in yRSC may be the Hlt1 subunit, although this cannot be fully confirmed via its limited resolution in 3D structural models.

Our studies initially focused on cBAF and PBAF complexes owing to the fact that SMARCE1 is only a member of these mSWI/SNF forms, and not the ncBAF complex (which lacks SMARCE1 along with several other cBAF/PBAF core members)[2,3]. However, genomic analyses revealed unexpected gains in mSWI/SNF genome-wide complex occupancy pointing toward a role for ncBAF, which we dissected at the biochemical and functional levels. These results underscore the importance of understanding the pathway and order-of-assembly for large, heterogeneous families of protein complexes, as without this, the biochemical basis for the increased ncBAF abundance and function would have been challenging to identify.

Although, at present, there are no cell line or xenograft models of CCM, the arachnoid cell (AC7) model we generated here highlights gene regulatory small-molecule sensitivities that suggest potential targeted biologic approaches. Given that chemical degraders of BRD9 as well as SMARCA4/2-specific ATPase inhibitors are now under evaluation in Phase I clinical trials (NCT04965753, NCT04891757), our findings provide the basis for potential inclusion of SMARCE1-deficient CCM, a cBAF-perturbed class of tumors that exhibit sensitivity to ncBAF and residual mSWI/SNF complex inhibition.

Online content

Any methods, additional references, Nature Research reporting summaries, source data, extended data, supplementary information, acknowledgements, peer review information; details of author contributions and competing interests; and statements of data and code availability are available at https://doi.org/10.1038/s41588-022-01077-0.

Received: 6 August 2021; Accepted: 12 April 2022;
Published online: 9 June 2022

References

1. Clapier, C. R., Iwasa, J., Cairns, B. R. & Peterson, C. L. Mechanisms of action and regulation of ATP-dependent chromatin-remodelling complexes. *Nat. Rev. Mol. Cell Biol.* **18**, 407–422 (2017).
2. Mashtalir, N. et al. Modular organization and assembly of SWI/SNF family chromatin remodeling complexes. *Cell* **175**, 1272–1288 e20 (2018).
3. Michel, B. C. et al. A non-canonical SWI/SNF complex is a synthetic lethal target in cancers driven by BAF complex perturbation. *Nat. Cell Biol.* **20**, 1410–1420 (2018).
4. Kadoch, C. et al. Proteomic and bioinformatic analysis of mSWI/SNF (BAF) complexes reveals extensive roles in human malignancy. *Nat. Genet.* **45**, 592–601 (2013).
5. Garraway, L. A. & Lander, E. S. Lessons from the cancer genome. *Cell* **153**, 17–37 (2013).
6. Pulice, J. L. & Kadoch, C. Composition and function of mammalian SWI/SNF chromatin remodeling complexes in human disease. *Cold Spring Harb. Symp. Quant. Biol.* **81**, 53–60 (2016).
7. Versteege, I. et al. Truncating mutations of hSNF5/INI1 in aggressive paediatric cancer. *Nature* **393**, 203–206 (1998).
8. Biegel, J. A. et al. Germ-line and acquired mutations of INI1 in atypical teratoid and rhabdoid tumors. *Cancer Res.* **59**, 74–79 (1999).
9. Storlazzi, C. T. et al. A novel fusion gene, *SS18L1/SSX1*, in synovial sarcoma. *Genes Chromosomes Cancer* **37**, 195–200 (2003).
10. Ramos, P. et al. Small cell carcinoma of the ovary, hypercalcemic type, displays frequent inactivating germline and somatic mutations in SMARCA4. *Nat. Genet.* **46**, 427–429 (2014).
11. Jones, S. et al. Frequent mutations of chromatin remodeling gene *ARID1A* in ovarian clear cell carcinoma. *Science* **330**, 228–231 (2010).
12. Sauter, J. L. et al. *SMARCA4*-deficient thoracic sarcoma: a distinctive clinicopathological entity with undifferentiated rhabdoid morphology and aggressive behavior. *Mod. Pathol.* **30**, 1422–1432 (2017).
13. Cao, S. et al. Comprehensive characterization of cancer driver genes and mutations. *Cell* **174**, 1034–1035 (2018).
14. Pan, J. et al. The ATPase module of mammalian SWI/SNF family complexes mediates subcomplex identity and catalytic activity-independent genomic targeting. *Nat. Genet.* **51**, 618–626 (2019).
15. Mashtalir, N. et al. A structural model of the endogenous human BAF complex informs disease mechanisms. *Cell* **183**, 802–817.e24 (2020).
16. Nakayama, R. T. et al. SMARCB1 is required for widespread BAF complex-mediated activation of enhancers and bivalent promoters. *Nat. Genet.* **49**, 1613–1623 (2017).
17. Wang, X. et al. SMARCB1-mediated SWI/SNF complex function is essential for enhancer regulation. *Nat. Genet.* **49**, 289–295 (2017).
18. Mathur, R. et al. ARID1A loss impairs enhancer-mediated gene regulation and drives colon cancer in mice. *Nat. Genet.* **49**, 296–302 (2017).
19. Kelso, T. W. R. et al. Chromatin accessibility underlies synthetic lethality of SWI/SNF subunits in ARID1A-mutant cancers. *eLife* **6**, e30506 (2017).
20. Smith, M. J. et al. Loss-of-function mutations in SMARCE1 cause an inherited disorder of multiple spinal meningiomas. *Nat. Genet.* **45**, 295–298 (2013).
21. Smith, M. J. et al. Germline SMARCE1 mutations predispose to both spinal and cranial clear cell meningiomas. *J. Pathol.* **234**, 436–440 (2014).
22. Gerkes, E. H. et al. A heritable form of SMARCE1-related meningiomas with important implications for follow-up and family screening. *Neurogenetics* **17**, 83–89 (2016).
23. Tauziede-Espariat, A. et al. Loss of SMARCE1 expression is a specific diagnostic marker of clear cell meningioma: a comprehensive immunophenotypical and molecular analysis. *Brain Pathol.* **28**, 466–474 (2018).
24. Inoue, T. et al. Hereditary clear cell meningiomas in a single family: three-cases report. *Acta Neurochir. (Wien.)* **160**, 2321–2325 (2018).
25. Libert, D. M. & Prayson, R. A. Pediatric clear cell meningioma involving the middle cranial fossa in the context of NF2 and SMARCE1 mutations. *Ann. Diagn. Pathol.* **46**, 151516 (2020).
26. Shoakazemi, A. et al. The importance of genetic counseling and screening for people with pathogenic *SMARCE1* variants: a family study. *Am. J. Med. Genet. A* **185**, 561–565 (2021).
27. Navalkele, P., Guzman, M., Kirby, A., Pinz, H. & Kemp, J. Familial pediatric clear cell meningioma with germline *SMARCE1* mutation in the United States. *J. Neuropathol. Exp. Neurol.* **79**, 1250–1252 (2020).
28. Sievers, P. et al. Clear cell meningiomas are defined by a highly distinct DNA methylation profile and mutations in *SMARCE1*. *Acta Neuropathol.* **141**, 281–290 (2021).
29. Smith, M. J. Germline and somatic mutations in meningiomas. *Cancer Genet.* **208**, 107–114 (2015).
30. Clark, V. E. et al. Genomic analysis of non-NF2 meningiomas reveals mutations in *TRAF7*, *KLF4*, *AKT1*, and *SMO*. *Science* **339**, 1077–1080 (2013).
31. Abedalthagafi, M. et al. Oncogenic PI3K mutations are as common as *AKT1* and *SMO* mutations in meningioma. *Neuro Oncol.* **18**, 649–655 (2016).
32. Bi, W. L., Prabhu, V. C. & Dunn, I. F. High-grade meningiomas: biology and implications. *Neurosurg. Focus* **44**, E2 (2018).
33. Ye, Y. et al. Structure of the RSC complex bound to the nucleosome. *Science* **366**, 838–843 (2019).

34. He, S. et al. Structure of nucleosome-bound human BAF complex. *Science* **367**, 875–881 (2020).
35. Han, Y., Reyes, A. A., Malik, S. & He, Y. Cryo-EM structure of SWI/SNF complex bound to a nucleosome. *Nature* **579**, 452–455 (2020).
36. Wagner, F. R. et al. Structure of SWI/SNF chromatin remodeller RSC bound to a nucleosome. *Nature* **579**, 448–451 (2020).
37. Estruch, F. & Carlson, M. SNF6 encodes a nuclear protein that is required for expression of many genes in *Saccharomyces cerevisiae*. *Mol. Cell. Biol.* **10**, 2544–2553 (1990).
38. Cairns, B. R., Kim, Y. J., Sayre, M. H., Laurent, B. C. & Kornberg, R. D. A multisubunit complex containing the SWI1/ADR6, SWI2/SNF2, SWI3, SNF5, and SNF6 gene products isolated from yeast. *Proc. Natl Acad. Sci. USA* **91**, 1950–1954 (1994).
39. Kadoch, C. & Crabtree, G. R. Mammalian SWI/SNF chromatin remodeling complexes and cancer: mechanistic insights gained from human genomics. *Sci. Adv.* **1**, e1500447 (2015).
40. Sen, P. et al. Loss of Snf5 induces formation of an aberrant SWI/SNF complex. *Cell Rep.* **18**, 2135–2147 (2017).
41. Beauchamp, R. L. et al. A high-throughput kinome screen reveals serum/glucocorticoid-regulated kinase 1 as a therapeutic target for NF2-deficient meningiomas. *Oncotarget* **6**, 16981–16997 (2015).
42. Vierbuchen, T. et al. AP-1 transcription factors and the BAF complex mediate signal-dependent enhancer selection. *Mol. Cell* **68**, 1067–1082.e12 (2017).
43. Pan, J. et al. Interrogation of mammalian protein complex structure, function, and membership using genome-scale fitness screens. *Cell Syst.* **6**, 555–568.e7 (2018).
44. Gatchalian, J. et al. A non-canonical BRD9-containing BAF chromatin remodeling complex regulates naive pluripotency in mouse embryonic stem cells. *Nat. Commun.* **9**, 5139 (2018).
45. Wang, X. et al. BRD9 defines a SWI/SNF sub-complex and constitutes a specific vulnerability in malignant rhabdoid tumors. *Nat. Commun.* **10**, 1881 (2019).
46. Remillard, D. et al. Degradation of the BAF complex factor BRD9 by heterobifunctional ligands. *Angew. Chem. Int. Ed. Engl.* **56**, 5738–5743 (2017).
47. Brien, G. L. et al. Targeted degradation of BRD9 reverses oncogenic gene expression in synovial sarcoma. *eLife* **7**, e41305 (2018).
48. Papillon, J. P. N. et al. Discovery of orally active inhibitors of brahma homolog (BRM)/SMARCA2 ATPase activity for the treatment of brahma related gene 1 (BRG1)/SMARCA4-mutant cancers. *J. Med. Chem.* **61**, 10155–10172 (2018).

Methods

All research performed as part of this study complied with all relevant ethical regulations set forth by the Office of Research Integrity at DFCI.

Experimental models. *Mammalian cell culture.* WT and SMARCE1-null HEK293T (human, ATCC, ACS-4500) cell lines were cultured in DMEM medium (Gibco) supplemented with 10% fetal bovine serum (Gibco), 1% GlutaMAX (Gibco), 1 mM HEPES pH 7.5 (Gibco), 1% sodium pyruvate (Gibco) and 1% penicillin–streptomycin (Gibco). AC7 arachnoid cell lines (AC-007-hTERT, derived from a patient with meningioma expressing WT levels of NF2) were a generous gift from V. Ramesh (Massachusetts General Hospital, Boston, MA). AC7 cells lines were cultured in DMEM medium (Gibco) supplemented with 15% fetal bovine serum (Gibco), 1% GlutaMAX (Gibco) and 1% penicillin–streptomycin (Gibco). The BT549 (Human, ATCC, HTB-122) cell line was cultured in RPMI 1640 medium (Gibco) supplemented with 15% fetal bovine serum (Gibco), 1% GlutaMAX (Gibco) and 1% penicillin–streptomycin (Gibco). All cell lines were maintained in a humidified incubator set at 37 °C with 5% CO_2. Cell lines used in this study were authenticated using the Dana-Farber Cancer Institute (DFCI) SNP testing protocol and were routinely tested for mycoplasma.

Human tumor and normal meninges specimens. Fresh-frozen tumor samples from normal meninges ($n=2$), *KLF4*/*TRAF7*-mutated meningiomas ($n=2$), *NF2*-mutated meningiomas ($n=7$) and *SMARCE1*-mutated CCM ($n=4$) were obtained from D. Meredith (Massachusetts General Hospital/ Brigham and Women's Hospital, Boston, MA) in accordance to local Institutional Review Board and HHS Office of Human Subjects Research Protections policy as prescribed by the National Institutes of Health. Clinical samples were kept anonymized and stored in −80 °C until processed for RNA isolation and RNA sequencing.

Stable gene expression construct and lentiviral infection. WT N-terminally V5-tagged SMARCE1 was constitutively expressed in the BT549 cell line using a modified pTight lentiviral system from Clontech with dual Promoter EF-1a-MCS-PGK-Puro. Lentivirus was generated by transfecting HEK293T LentiX cells (Clontech) with V5 SMARCE1 construct along with packaging vectors pspax2 and pMD2.G in the presence of polyethylenimine (Polysciences). At 72 h post-transfection, viral medium was clarified with 0.45-μM vacuum filter (Millipore Sigma), and concentrated by ultracentrifugation at 40,000*g* for 2.5 h at 4 °C. The viral pellet was resuspended in PBS and used to infect BT549 with 10 μg ml^{-1} protamine sulfate (Sigma-Aldrich). Overexpression was confirmed by western blot analysis.

Protein extraction methods. Mammalian cell cultures were grown to confluence under standard conditions, trypsinized and washed with PBS before being subjected to protein extractions.

For whole-cell extracts, cells were resuspended in approximately three to five volumes of SDS extraction buffer (20 mM Tris and 1.5% SDS) at room temperature. Samples were solubilized through sonication and heated at 95 °C for 3 min. Protein concentration was assessed using bicinchoninic acid assay (BCA).

For nuclear extraction, protein was extracted by performing ammonium sulfate nuclear extraction as previously reported[49]. Briefly, cells were resuspended in hypotonic buffer A (10 mM HEPES pH 7.6, 25 mM KCl, 1 mM EDTA, 10% glycerol) supplemented with 1 mM dithiothreitol and protease inhibitors (cOmplete Mini tablets (Roche) supplemented with 1 mM phenylmethyl sulfonyl fluoride). Following a short incubation on ice, nuclei were pelleted (1,000*g* for 5 min), and lysed in buffer C (10 mM HEPES pH 7.6, 3 mM $MgCl_2$, 100 mM KCl, 0.1 mM EDTA, 10% glycerol) supplemented with 1 mM dithiothreitol, protease inhibitor, and 0.3 M ammonium sulfate. The insoluble chromatin fraction was sedimented by centrifugation (30,000*g* for 30 min), and precipitated by adding ammonium sulfate to a final concentration of 0.3 mg ml^{-1} for 20 min on ice. The nuclear protein precipitate was recovered by centrifugation (30,000*g* for 30 min), and kept at −80 °C until use.

Immunoprecipitation. Stored nuclear extract pellets were resuspended in EB300 buffer (50 mM Tris pH 7.5, 300 mM NaCl, 1% NP-40, 1 mM EDTA, 1 mM $MgCl_2$) supplemented with 1 mM dithiothreitol, protease inhibitors and 1 mM phenylmethyl sulfonyl fluoride, followed by quantification using BCA. IP was carried out using approximately 300–500 μg of protein with 2–5 μg of antibody or with 25 μl of Pierce anti-hemagglutinin (HA) magnetic beads with overnight rotation at 4 °C. When free antibody was used for IP, antibody-bound complex was captured with 30 μl Protein G Dynabeads (ThermoFisher Scientific) for 2 h at 4 °C with constant rotation. Bead-bound complexes were washed five times with complete EB300 buffer, eluted with fresh sample buffer (2× NuPAGE LDS buffer with 100 mM dithiothreitol) and loaded onto 4%–12% Bis–Tris NuPAGE Gels (Life Technologies). See Supplementary Table 4 for the antibodies used in this study.

Density sedimentation. Nuclear extracts were resuspended in BC0 buffer (25 mM HEPES pH 7.9, 0.1 mM EDTA, 12.5 mM $MgCl_2$, 100 mM KCl) supplemented with 1 mM dithiothreitol, protease inhibitors and 1 mM phenylmethyl sulfonyl fluoride, followed by quantification using BCA. For each sedimentation run, 1 mg of protein was loaded on top of a linear 10%–30% glycerol gradients with BC0 as the base buffer. Glycerol gradient tubes were loaded into a SW41 rotor and centrifuged at 20,000*g* for 16 h at 4 °C. Following centrifugation, sample was aliquoted in 550 μl fractions. Between 100 and 250 μl of each aliquoted fraction were concentrated using 10–15 μl of Strataclean beads with constant rotation for 2 h at 4 °C. The protein-bound beads were eluted in fresh sample buffer (2× NuPAGE LDS buffer with 100 mM dithiothreitol) and loaded onto 4%–12% Bis–Tris NuPAGE Gels (Life Technologies). Samples assessed by SDS–PAGE gels were stained using Silver Quest staining kit, or further processed for western blot analysis.

Western blotting. Western blot analysis was carried out using standard protocols. Boiled samples were loaded on 4%–12% PAGE gel, separated with constant 150 V for 60–90 min at room temperature. Separated protein sample was transferred to the appropriate polyvinylidene difluoride membrane at 250–300 mA for 2 h at 4 °C. Membranes were blocked with 5% milk in PBST for 1 h and incubated (1:1,000) with primary antibodies overnight. Membranes were then washed three times with fresh PBST, incubated with LI-COR compatible secondary antibodies (1:10,000) with gentle rocking for 1 h at room temperature. Lastly, membranes were washed three times with PBST, and imaged using LI-COR Odyssey CLx. Antibodies used are detailed in Supplementary Table 4. For primary antibodies, we used a 1:1,000 or 1:2,000 dilution, and used the secondary antibodies at 1:10,000.

Large-scale complex variant purification. Variants of the mSWI/SNF complexes were purified as described, with modifications detailed below[2]. Both WT and SMARCE1-deficient 293T cell lines expressing full-length HA–SMARCD1 constructs were cultured in parallel in 150-mm dishes and expanded to 100 plates. At 90%–95% confluency, cells were scraped, washed with cold PBS, and lysed with hypotonic buffer containing 10 mM Tris–HCl pH 7.5, 10 mM KCl, 1.5 mM $MgCl_2$, supplemented with 1 mM dithiothreitol, protease inhibitors and 1 mM phenylmethyl sulfonyl fluoride. The cytoplasmic suspensions were incubated on ice for 10 min, pelleted and resuspended in high-salt buffer containing 50 mM Tris–HCl pH 7.5, 300 mM KCl, 1 mM $MgCl_2$, 1 mM EDTA, 1 mM, 1% NP-40, supplemented with 1 mM dithiothreitol, protease inhibitors and 1 mM phenylmethyl sulfonyl fluoride. The nuclear suspensions were incubated on a rotator for 1 h, and spun down at 30,000*g* for 1 h at 4 °C using a SW32Ti rotor to remove the insoluble chromatin pellet. The soluble nuclear extract was filtered through a 0.45-μm filter, and incubated with 500 μl of anti-HA beads (Pierce, catalog no. 88836) per 50 dishes. Following overnight incubation at 4 °C with continuous rotation, mSWI/SNF complexes were eluted with HA peptide, concentrated and loaded onto a glycerol gradient for density sedimentation (see method above for details).

REAA and ATPase assays. Complexes were isolated from 100–200 μg of ammonium sulfate-precipitated nuclear extracts, using 100–150 ng of antibodies specific for ARID1A, ARID2, SMARCA4, SS18 and IgG, and incubated overnight at 4 °C. The associated complexes and IgG controls were precipitated with Protein G Dynabeads and washed three times with high-salt buffer 1 (50 mM Tris–HCl, pH 7.5, 300 mM KCl, 1% NP-40, supplemented with protease inhibitor) and three times with high-salt buffer 2 (50 mM Tris–HCl, pH 7.5, 300 mM NaCl, 1% NP-40, supplemented with protease inhibitor). Following extensive salt washes, the Protein G Dynabead-bound complexes were washed once in REAA/ATPase wash buffer (20 mM HEPES, pH 8.0, 50 mM KCl, 5 mM $MgCl_2$, 1 mM dithiothreitol) and resuspended in complete REAA/ATPase reaction buffer (20 mM HEPES, pH 8.0, 50 mM KCl, 5 mM $MgCl_2$, 1 mM dithiothreitol, 0.1 mg ml^{-1} BSA, 5 nM Widom 601 sequence mononucleosomes (Epicypher), 0.3–1 mM ATP and 1–2 units of DpnII). Enzymatic reactions were incubated on an Eppendorf ThermoMixer C with a 96-well plate adapter and vortexed at 600*g* for 60–90 min at 37 °C. To assess dual ATPase and remodeling activity, the reactions were equally partitioned. One set underwent ADP concentration measurements with ADP-Glo (Promega) and the remaining aliquot was subjected to Proteinase K digestion for 60 min at 55 °C on a PCR thermocycler. The liberated DNA was precipitated with SPRI beads and the restriction enzyme-digested DNA was assessed with the automated electrophoresis TapeStation system (Agilent). Immunoblotting with a subset of material and normalization to epitope bait levels using quantitative densitometry (LI-COR software) was used to normalize amounts of immunoprecipitated material for each epitope used in the assay. The ATPase/REAA reactions were performed in quadruplicate and data were plotted in bar graphs and subjected to statistical analysis on GraphPad Prism.

Generation of AC7 cell SMARCE1 KO and confirmation method. *SMARCE1* crRNA was purchased from IDT, annealed with tracrRNA (IDT 1072533), and incubated with Alt-R S.p. HiFi Cas9 Nuclease (IDT 1078727) resulting in Cas9-SMARCE1-gRNA ribonucleoprotein for gene specific editing. Predesigned Alt-R CRISPR–Cas9 gRNA for SMARCE1: Hs.Cas9.SMARCE1.1.AA (TTATGTAAGCAAGGTACGCG), Hs.Cas9.SMARCE1.1.AB (AATGCAGGTCCTCAAACGGC), Hs.Cas9.SMARCE1.1.AC (TTTTGGAATCGTGATACCAG). Three *SMARCE1* crRNA along the length of the gene to maximize target genomic deletions. Resulting ribonucleoprotein was transfected with Lipofectamine RNAiMAX (ThermoFisher Scientific, catalog

no. 13778030). Transfected cells were incubated for 2 d and diluted to a ratio of 0.5 cells per well of a 96-well plate. Single-cell clones were isolated over a period of three weeks and screened for loss of SMARCE1 using total cell immunoblot and sequencing.

ChIP–seq sample preparation. Cells were trypsinized, washed with room temperature PBS twice to remove trypsin, and divided into aliquots of 40 million cells. Cells were fixed using 1% formaldehyde (Sigma-Aldrich) for 10 min at 37 °C with constant stirring to keep cells in solution, and finally quenched with 125 mM glycine for 5 min at 37 °C. Quenched cells were washed with cold PBS, and stored in 10-million aliquots at −80 °C until they were used. Ten million cells were used per epitope in subsequent ChIPs. Following nuclei extraction, chromatin was sonicated using a Covaris E220 Focused-Ultrasonicator system. Sonicated chromatin was cleared by centrifugation for 10 min at 15,000*g*. Soluble fractions were incubated with the indicated antibodies (see antibody list, with 2–3 µg of antibody) overnight at 4 °C, and captured using Protein G Dynabeads (ThermoFisher Scientific). All ChIP–seq samples received 20 ng of spike-in *Drosophila* chromatin (Active Motif), and 2 µg spike-in antibody (Active Motif) for normalization after sequencing. Antibody–chromatin complexes were captured with Protein G Dynabeads (ThermoFisher Scientific), washed extensively, eluted, and treated with RNase A (Roche) for 30 min at 37 °C and Proteinase K (Life Technologies) for 3 h at 65 °C. ChIP DNA samples were extracted using SPRI beads (Beckman Coulter Agencourt AMP Xpure), washed with 80% ethanol, and eluted using 0.1× TE. ChIP DNA samples were stored at −20 °C before library preparations were initiated. All ChIP–seq libraries were processed with Illumina's NEBNext Ultra II DNA Library Prep Kit (following standard protocols). All ChIP–seq libraries were sequenced on the Illumina NextSeq 500 with 75-bp single-end sequencing.

ATAC-seq. The omni ATAC-seq protocol was used with slight modifications, as detailed below[50]. Between 50,000 and 100,000 cells were trypsinized and washed with cold PBS to remove trypsin. When appropriate, lysing steps were carried out in 10× bulk. Cell pellets were resuspended in 50 µl of cold ATAC-seq resuspension buffer containing 10 mM Tris–HCl pH 7.4, 10 mM NaCl and 3 mM $MgCl_2$, supplemented with fresh NP-40 (final 0.1% v/v), Tween-20 (final 0.1% v/v) and digitonin (final 0.01% v/v). Resuspended cells were incubated in lysis buffer for 3–5 min on ice. The lysis step was quenched with 1 ml of resuspension buffer supplemented with Tween-20 (final 0.1% v/v) and pelleted at 500*g* for 10 min at 4 °C. Cell pellets were resuspended in 50 µl of transposition reaction mix containing 25 µl of 2× TD buffer, 2.5 µl of transposase, 16.5 µl of 1× PBS, 0.5 µl of 1% digitonin (final 0.01% v/v), 0.5 µl of 10% Tween-20 (final 0.1% v/v) and 5 µl of nuclease-free water. The transposition reaction was assembled, mixed and incubated at 37 °C for 30 min with constant shaking on a thermomixer. To purify the tagmented DNA, a Qiagen MinElute Reaction Cleanup Kit was used. A standard ATAC-seq amplification protocol with 10–12 cycles of amplification was used to amplify the tagmented library[51]. ATAC-seq libraries were sequenced on NextSeq 500 (Illumina) using 37-bp paired-end sequencing.

RNA-seq from cell cultures. One million cells were trypsinized and washed with cold PBS to remove trypsin. RNA was purified using the Qiagen RNeasy kit, and further processed in the Illumina TruSeq Stranded mRNA Library Prep Kit with appropriate RNA spike-in to mitigate experimental errors. All RNA-seq samples were analyzed using TapeStation to assess quality, and a Qubit Fluorometer to measure concentration. All ChIP–seq libraries were sequenced on the Illumina NextSeq 500 with 75-bp single-end sequencing.

RNA isolation from primary tumors. Between 15 and 25 mg of fresh-frozen tissue samples were harvested on ice and washed with cold PBS. Samples were immediately resuspended in cold Qiagen proprietary RLT buffer. The tissue was initially grinded within a 1.5-ml Eppendorf tube with a small pestle, and further homogenized using a QiaShredder. Remaining steps were followed as done with the Qiagen RNeasy kit.

CUT&Tag. CUT&Tag was carried out according to Epicypher's protocol in 8-strip PCR tubes with slight modifications. Concanavalin A-coated magnetic beads were activated with bead activation buffer containing 20 mM HEPES, pH 7.9, 10 mM KCl, 1 mM $CaCl_2$, 1 mM $MnCl_2$; beads were kept at room temperature until use. 100,000 cells were trypsinized and washed with cold PBS to remove trypsin. Cells were lysed sing cold nuclear extraction buffer containing 20 mM HEPES–KOH, pH 7.9, 10 mM KCl, 0.1% Triton X-100 and 20% glycerol supplemented with fresh 0.5 mM spermidine, and cOmplete Mini, EDTA-free protease inhibitor (Roche). Samples of nuclei were incubated with activated concanavalin A beads at room temperature for 10 min. The nuclei–concanavalin A bead complex was resuspended in Antibody 150 buffer containing 20 mM HEPES, pH 7.5, 150 mM NaCl, supplemented with fresh 0.5 mM spermidine protease inhibitor (Roche), 0.01% digitonin and 500 ng of primary antibody (see Supplementary Table 4). Following overnight incubation at 4 °C, primary antibody was removed and beads were washed once with digitonin 150 buffer containing 20 mM HEPES, pH 7.5, 150 mM NaCl, supplemented with fresh 0.5 mM spermidine protease inhibitor (Roche) and 0.01% digitonin. Secondary antibody was added, and incubated with the nuclei–concanavalin A bead complex for 1 h at room temperature. The nuclei–concanavalin A bead complex was washed with digitonin 150 buffer twice before resuspension in 50 µl of cold digitonin 300 buffer containing 20 mM HEPES, pH 7.5, 300 mM NaCl, supplemented with fresh 0.5 mM spermidine protease inhibitor (Roche) and 0.01% digitonin. Two microliters of CUTANA pAG-Tn5 (Epicypher) was added to each sample and incubated on a nutator for 1 h at room temperature. Following incubation, beads were washed with cold digitonin 300 buffer. Targeted chromatin tagmentation and library amplification were carried out in accordance with Epicypher's protocol.

Analysis of CX-MS data and structural data. Raw cross-link counts for SMARCE1 residues were normalized to the total cross-link count in the BAF apo, BAF-NCP and PBAF CX-MS datasets[2,15] and this ratio was plotted along with SMARCE1 in stacked bar plots, broken down by cross-linked subunits (that is the *y* axis represents the percentage of cross-links of a specific SMARCE1 residue to any of the BAF/PBAF subunits in the dataset). Next, these counts were normalized to the total number of cross-link counts in the entire dataset given that the CX-MS studies for cBAF and PBAF captured different total numbers of cross-links. Data visualization on the ySWI/SNF, yRSC and cBAF complexes was carried out using the USCF Chimera visualization tool[52]. Each subunit is color coded and lysine (K) residues of interest are shown in black on SMARCE1 and in red for other mSWI/SNF subunit lysine residues.

Drug treatment with BRD9 degrader (dBRD9A) and ATPase inhibitor (CMP12). Cells were seeded in 384- or 96-well plates and were treated with dBRD9A (Tocris, catalog no. 6943) and CMP12 (synthesized in J. Qi's laboratory at DFCI) at the indicated concentrations over the course of the days indicated. Medium containing new compound was refreshed every 3 d for experiments that lasted more than 3 d. Impact on cell proliferation was measured using the luminescent detection system CellTiter-Glo Luminescent Cell Viability Assay (Promega, catalog no. G7571) at the indicated time points.

NGS data processing. CUT&Tag, ChIP–seq, ATAC-seq and RNA-seq samples were sequenced using Illumina NextSeq 500 technology, and output data were demultiplexed using the bcl2fastq software tool v.2.20 (Illumina). RNA-seq reads were aligned to the hg19 genome with STAR v.2.5.2b (ref. [53]), and tracks were generated using the deepTools v2.5.3 bamCoverage function[54]. ChIP–seq reads were aligned with Bowtie2 v.2.29 (ref. [55]) in the -k 1 reporting mode, and narrow peaks were called with MACS2 v.2.1.1 software using a *q*-value cutoff of 0.001 (ref. [56]). For ATAC-seq data, quality read trimming was carried out by Trimmomatic v.0.36 (ref. [57]), followed by alignment, duplicate read removal and read-quality filtering using Bowtie2, Picard v.2.8.0 (refs. [58–60]) and SAMtools v .0.1.19 (ref. [59]), respectively. ATAC-seq broad peaks were called with MACS2 using the BAMPE option and a broad peak cutoff of 0.001. For ChIP–seq and ATAC-seq track generation, output BAM files were converted into BigWig files using MACS2 and UCSC utilities[61] in order to display coverage throughout the genome in reads per million values. For CUT&Tag libraries, the CutRunTools pipeline was leveraged to perform read trimming, quality filtering, alignment, peak calling and track building using default parameters[62].

RNA-seq data analysis. For RNA-seq data, output gene count tables from STAR based on alignments to the hg19 reflat annotation were used as input into edgeR v.3.12.1 (ref. [60]) to evaluate differential gene expression. $\log_2$(fold change) values from edgeR were used as input into GSEA[63], and the GseaPreranked tool was run with default settings to measure gene set enrichment. To analyze gene set or pathway enrichment for select subsets of genes, either Metascape was used[64] or hypergeometric tests were performed on overlaps with MSIGDB Wikipathway gene sets. In gene expression heatmaps, RPKM values were quantified using median length isoforms and total mapped read counts computed by the SAMtools idxstats function, and these RPKMs were transformed into Z-scores followed by K-means clustering. PCA was performed using the wt.scale and fast.svd functions from the corpcor R package on RPKM values[65,66].

ChIP–seq, CUT&Tag and ATAC-seq data analysis. Heatmaps and metaplots displaying signals aligned with peak centers were generated using ngsplot v.2.63 (ref. [67]). In several heatmaps, K-means clustering was applied to partition the data into groups. The R package, ChIPpeakAnno v.3.17.0, was used to visualize peak overlaps, and the BEDtools multiIntersectBed and merge functions were used for peak merging[68]. In these heatmaps, ChIP–seq and CUT&Tag samples (with the same antibodies) and ATAC-seq samples were scaled separately but on equal levels across conditions (using reads per million or log(fold change) over input values). Distances to TSS peak distributions were computed utilizing Ensembl protein coding gene coordinates provided by ngsplot. Transcription factor enrichment and motif analyses were carried out using the LOLA v.1.12.0 (ref. [69]) and HOMER v.4.9 (ref. [70]) software packages, respectively. *Cis*-regulatory function was assessed by GREAT[71], and chromVAR[72] was used to detect motif enrichment over sites of variable accessibility or chromatin factor occupancy. To evaluate differential accessibility at sites between conditions, paired-end read fragment counts from

ATAC-seq samples within given peaks were computed using the BEDTools intersect function, and these counts were input into edgeR.

Additional transcription factor motif enrichment analyses. In addition to using HOMER to analyze motif enrichment, for several motif enrichment analyses conducted in this study, we determined the number of motif occurrences for 286 nonredundant archetype consensus motifs[73] within ±250 bp of peak centers for each peak within given peak sets. The coordinates of these archetype motifs across the entire human genome can be downloaded from the following resource https://www.vierstra.org/resources/motif_clustering#downloads.

To measure the relationship between the motif counts and changes in SMARCA4 occupancy or ATAC-seq accessibility levels, we determined the $\log_2$(fold change) distributions between conditions as a function of motif count per site for each transcription factor archetype motif and then computed median $\log_2$(fold change) values for sites with 0–5 motif counts. If fewer than 100 sites were associated with a certain motif count for a certain motif, then the data were discarded for that archetype's motif count.

Reporting summary. Further information on research design is available in the Nature Research Reporting Summary linked to this article.

Data availability

All genomic data contained in this manuscript have been deposited on the Gene Expression Omnibus (GEO) repository, https://www.ncbi.nlm.nih.gov/geo/, under accession code GSE174360. Source data are provided with this paper or are provided as Supplementary Information. Raw sequencing data from the fresh-frozen primary meningioma tumor samples (controlled access samples) can be made available upon request to C. Kadoch and D. Meredith, with a time frame for response of 1–2 days, and data availability within 2–3 weeks.

Code availability

No custom code was generated for this study.

References

49. Kadoch, C. & Crabtree, G. R. Reversible disruption of mSWI/SNF (BAF) complexes by the SS18-SSX oncogenic fusion in synovial sarcoma. *Cell* **153**, 71–85 (2013).
50. Corces, M. R. et al. An improved ATAC-seq protocol reduces background and enables interrogation of frozen tissues. *Nat. Methods* **14**, 959–962 (2017).
51. Buenrostro, J. D., Wu, B., Chang, H. Y. & Greenleaf, W. J. ATAC-seq: a method for assaying chromatin accessibility genome-wide. *Curr. Protoc. Mol. Biol.* **109**, 21.29.1–21.29.9 (2015).
52. Pettersen, E. F. et al. UCSF Chimera–a visualization system for exploratory research and analysis. *J. Comput Chem.* **25**, 1605–1612 (2004).
53. Dobin, A. et al. STAR: ultrafast universal RNA-seq aligner. *Bioinformatics* **29**, 15–21 (2013).
54. Ramírez, F. et al. deepTools2: a next generation web server for deep-sequencing data analysis. *Nucleic Acids Res.* **44**, W160–W165 (2016).
55. Langmead, B. & Salzberg, S. L. Fast gapped-read alignment with Bowtie 2. *Nat. Methods* **9**, 357–359 (2012).
56. Zhang, Y. et al. Model-based analysis of ChIP-Seq (MACS). *Genome Biol.* **9**, R137–R137 (2008).
57. Bolger, A. M., Lohse, M. & Usadel, B. Trimmomatic: a flexible trimmer for Illumina sequence data. *Bioinformatics* **30**, 2114–2120 (2014).
58. Picard. http://broadinstitute.github.io/picard/ or https://github.com/broadinstitute/picard
59. Li, H. et al. The sequence alignment/map format and SAMtools. *Bioinformatics* **25**, 2078–2079 (2009).
60. Zhu, Q., Liu, N., Orkin, S. H. & Yuan, G.-C. CUT&RUNTools: a flexible pipeline for CUT&RUN processing and footprint analysis. *Genome Biol.* **20**, 192–192 (2019).
61. Robinson, M. D., McCarthy, D. J. & Smyth, G. K. edgeR: a Bioconductor package for differential expression analysis of digital gene expression data. *Bioinformatics* **26**, 139–140 (2010).
62. Kuhn, R. M., Haussler, D. & Kent, W. J. The UCSC genome browser and associated tools. *Brief. Bioinforma.* **14**, 144–161 (2013).
63. Subramanian, A. et al. Gene Set enrichment analysis: a knowledge-based approach for interpreting genome-wide expression profiles. *Proc. Natl Acad. Sci. USA* **102**, 15545–15550 (2005).
64. Tripathi, S. et al. Meta- and orthogonal integration of influenza "OMICs" data defines a role for UBR4 in virus budding. *Cell Host Microbe* **18**, 723–735 (2015).
65. Schäfer, J. & Strimmer, K. A shrinkage approach to large-scale covariance matrix estimation and implications for functional genomics. *Stat. Appl. Genet. Mol. Biol.* **4**, 32 (2005).
66. Opgen-Rhein, R. & Strimmer, K. Accurate ranking of differentially expressed genes by a distribution-free shrinkage approach. *Stat. Appl. Genet. Mol. Biol.* **6**, 9 (2007).
67. Shen, L., Shao, N., Liu, X. & Nestler, E. ngs.plot: quick mining and visualization of next-generation sequencing data by integrating genomic databases. *BMC Genom.* **15**, 284–284 (2014).
68. Quinlan, A. R. & Hall, I. M. BEDTools: a flexible suite of utilities for comparing genomic features. *Bioinformatics* **26**, 841–842 (2010).
69. Sheffield, N. C. & Bock, C. LOLA: enrichment analysis for genomic region sets and regulatory elements in R and Bioconductor. *Bioinformatics* **32**, 587–589 (2016).
70. Heinz, S. et al. Simple combinations of lineage-determining transcription factors prime cis-regulatory elements required for macrophage and B Cell Identities. *Mol. Cell* **38**, 576–589 (2010).
71. Schaar, B. T. et al. GREAT improves functional interpretation of cis -regulatory regions. *Nat. Biotechnol.* **28**, 495–501 (2010).
72. Schep, A. N., Wu, B., Buenrostro, J. D. & Greenleaf, W. J. chromVAR: inferring transcription-factor-associated accessibility from single-cell epigenomic data. *Nat. Methods* **14**, 975–978 (2017).
73. Vierstra, J. et al. Global reference mapping of human transcription factor footprints. *Nature* **583**, 729–736 (2020).

Acknowledgements

We thank all members of the Kadoch laboratory for thoughtful discussions throughout the duration of this project. We are grateful to Z. Herbert and M. Sullivan of the DFCI Molecular Biology Core Facility (MBCF) for help with high-throughput sequencing studies. We are grateful to M. Leidl for technical assistance in SMARCE1 cloning and biochemical experiments. We thank N. Gray for the synthesis and scale-up of dBRD9A. This study was supported in part by the Landry Cancer Consortium Award (R.S.P.), the National Institutes of Health 5F31CA228441-02 (R.S.P.), grants 1DP2CA195762-01 (C.K.), the Pew-Stewart Scholars in Cancer Research Award (C.K.), American Brain Tumor Association (ABTA), the American Cancer Society Research Scholar Award RSG-14-051-01-DMC (C.K.), the all-Manchester National Institute for Health and Care Research (NIHR) Biomedical Research Centre (IS-BRC-1215-20007) (M.J.S.), and the U.S. Army Medical Research Acquisition Activity Congressionally Directed Medical Research Program (USAMRAA CDMRP) Neurofibromatosis Research Program, Investigator-Initiated Research Award (W81XWH1910334) (M.J.S.).

Author contributions

R.S.P., C.J.W. and C.K. conceived of the study. R.S.P. performed all experiments with help from C.J.W., D.D.S.G., O.B. and N.M. All computational analyses were performed by C.K.C., with help from A.S. for cross-linking mass spectrometry and structural analyses. Cmp12 was synthesized and validated by Y.L. with oversight from J.Q., M.J.S., E.H.G., W.L.B. and D.M.M. identified and collected primary tumor and normal human tissue for DNA and RNA sequencing. V.R. provided the AC7 arachnoid cell line, the AC7 NF2-deleted cell line, and guidance for CRISPR–Cas9-mediated editing experiments. C.K. supervised the study. R.S.P., C.K. and C.K.C. wrote and edited the paper.

Competing interests

C.K. is the scientific founder, Fiduciary Board of Directors member, Scientific Advisory Board member, shareholder and consultant for Foghorn Therapeutics, Inc. (Cambridge, MA). C.K. is also a member of the Scientific Advisory Boards of Nereid Therapeutics and Nested Therapeutics, and serves as a consultant for Cell Signaling Technologies. All other authors do not declare any competing interests.

Additional information

Extended data is available for this paper at https://doi.org/10.1038/s41588-022-01077-0.

Supplementary information The online version contains supplementary material available at https://doi.org/10.1038/s41588-022-01077-0.

Correspondence and requests for materials should be addressed to Cigall Kadoch.

Peer review information *Nature Genetics* thanks Blaine Bartholomew, Tom Owen-Hughes and the other, anonymous, reviewer(s) for their contribution to the peer review of this work.

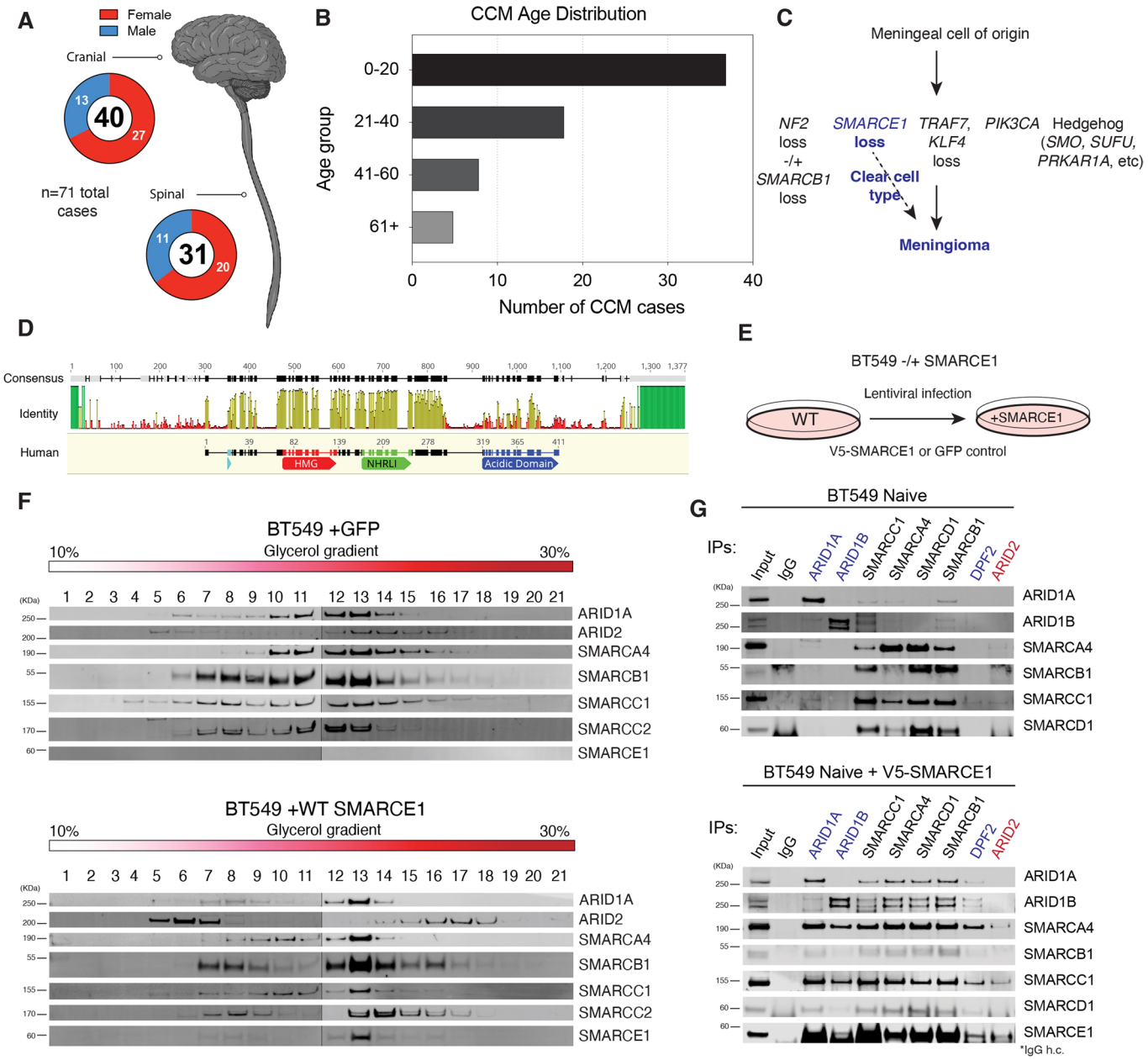

Extended Data Fig. 1 | CCM-associated loss of SMARCE1 selectively impacts the cBAF assembly of mSWI/SNF complexes. a. Distribution of cranial and spinal SMARCE1-deficient clear cell meningioma reported in the literature; male and female cases indicated in legend. Image adapted from 'CNS (lateral, no nerves)', by BioRender.com (2022). Retrieved from https://app.biorender.com/biorender-templates. **b**. Age distribution among SMARCE1-deficient CCM cases (n = 71); median= 10.8 years. **c**. Frequently mutated genes and their associated pathways in meningioma. SMARCE1 loss uniformly defines the clear cell meningioma subtype. **d**. Domain architecture and conservation of the human SMARCE1 protein. **e**. Schematic for SMARCE1 rescue experiments in BT549 SMARCE1-deificient cells. **f**. Density sedimentation experiments using 10–30% glycerol gradients performed on nuclear extracts isolated from BT549 cells infected with either empty vector control or WT SMARCE1. **g**. Lentiviral expression of SMARCE1 (or GFP control) in BT549 (SMARCE1 -/-) cells, followed by IP-western blotting for mSWI/SNF complex subunits. *IgG h.c. indicates IgG heavy chain bands are present. (f-g), representative of n = 3 experiments with similar results.

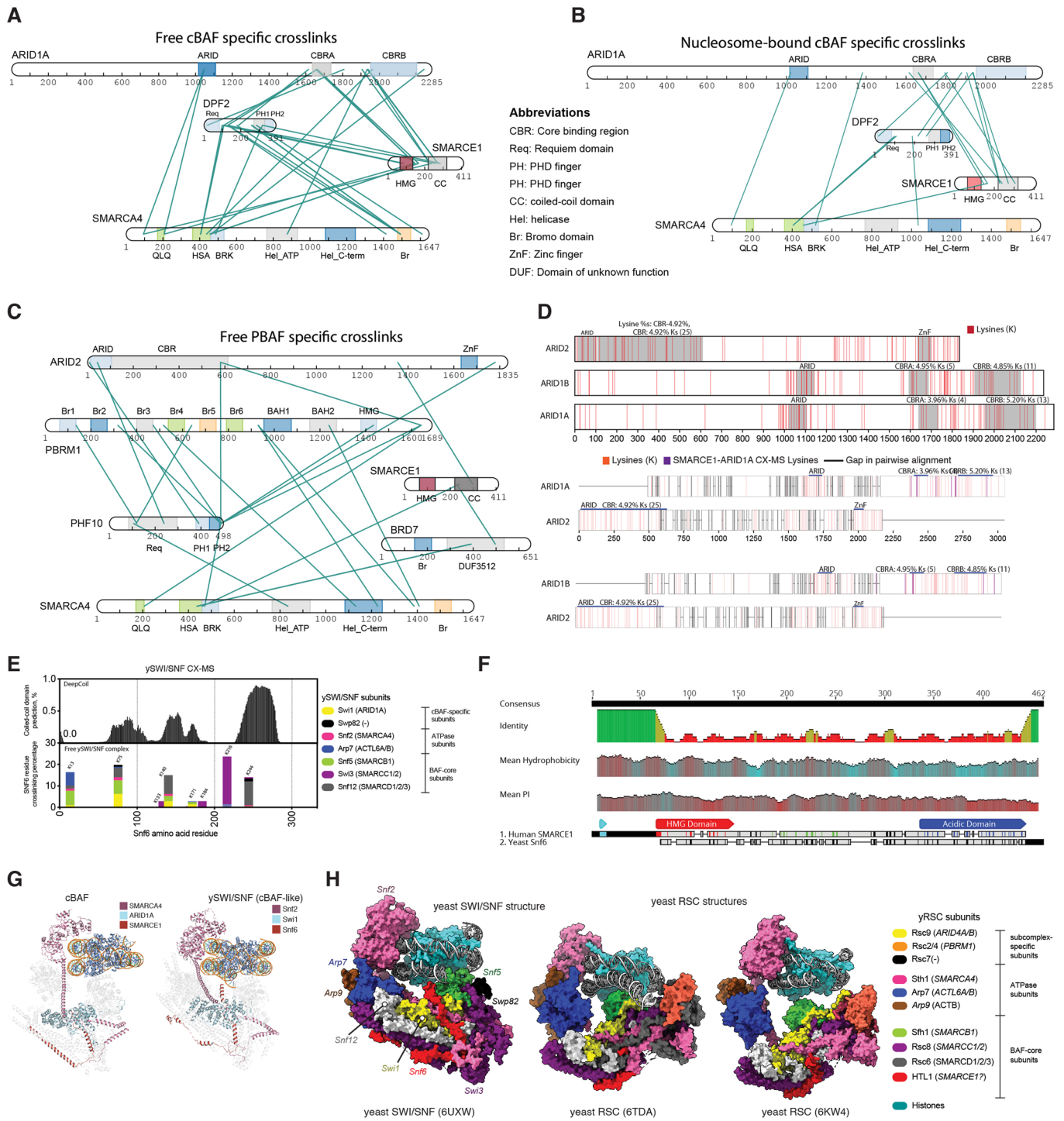

Extended Data Fig. 2 | SMARCE1 has structural homology to ySnf6 and tethers to the initial core of cBAF and PBAF complexes, but to ARID1A and SMARCA4 only in cBAF complexes. a,**b**. CX-MS analyses performed on (A) apo human canonical BAF (cBAF), and (B) NCP-bound cBAF complexes. SMARCE1, cBAF-specific subunits (ARID1A and DPF2), and the ATPase subunit, SMARCA4, are shown. **c**. CX-MS analyses performed on apo human PBAF complexes. SMARCE1, PBAF-specific subunits (ARID2, PBRM1, BRD7 and PHF10), and the ATPase, SMARCA4, are shown. **d**. Top, Number and distribution of lysine (K) residues (red) on ARID1A/B and ARID2 subunits. Core binding region (CBR) on each is indicated. Bottom, pairwise alignment between ARID1A/B and ARID2 with SMARCE1-ARID1A CX-MS sites highlighted (purple). **e**. Cross-linking mass spec analyses performed on ySWI/SNF complexes in nucleosome-unbound states [Sen et al., 2017; Mashtalir et al., 2018]. Crosslinks are plotted as a percentage of total crosslinks recovered in the dataset, and are marked by the ySWI/SNF subunit to which they tether (legend). Selected crosslinked lysine (K) residues of Snf6 are labeled. DeepCoil coiled-coil prediction scores are indicated on top row. **f**. Amino acid sequence conservation of human SMARCE1 to yeast Snf6. **g**. Human cBAF (PDB: 6LTJ) structure contrasted to cBAF-like yeast SWI/SNF (PDB: 6UXW). **h**. Cryo-EM structures of ySWI/SNF (PDB: 6UXW) and yRSC (PDB: 6TDA and PDB: 6KW4). Putative SMARCE1 homologs, Snf6 and Htl1, are highlighted in red.

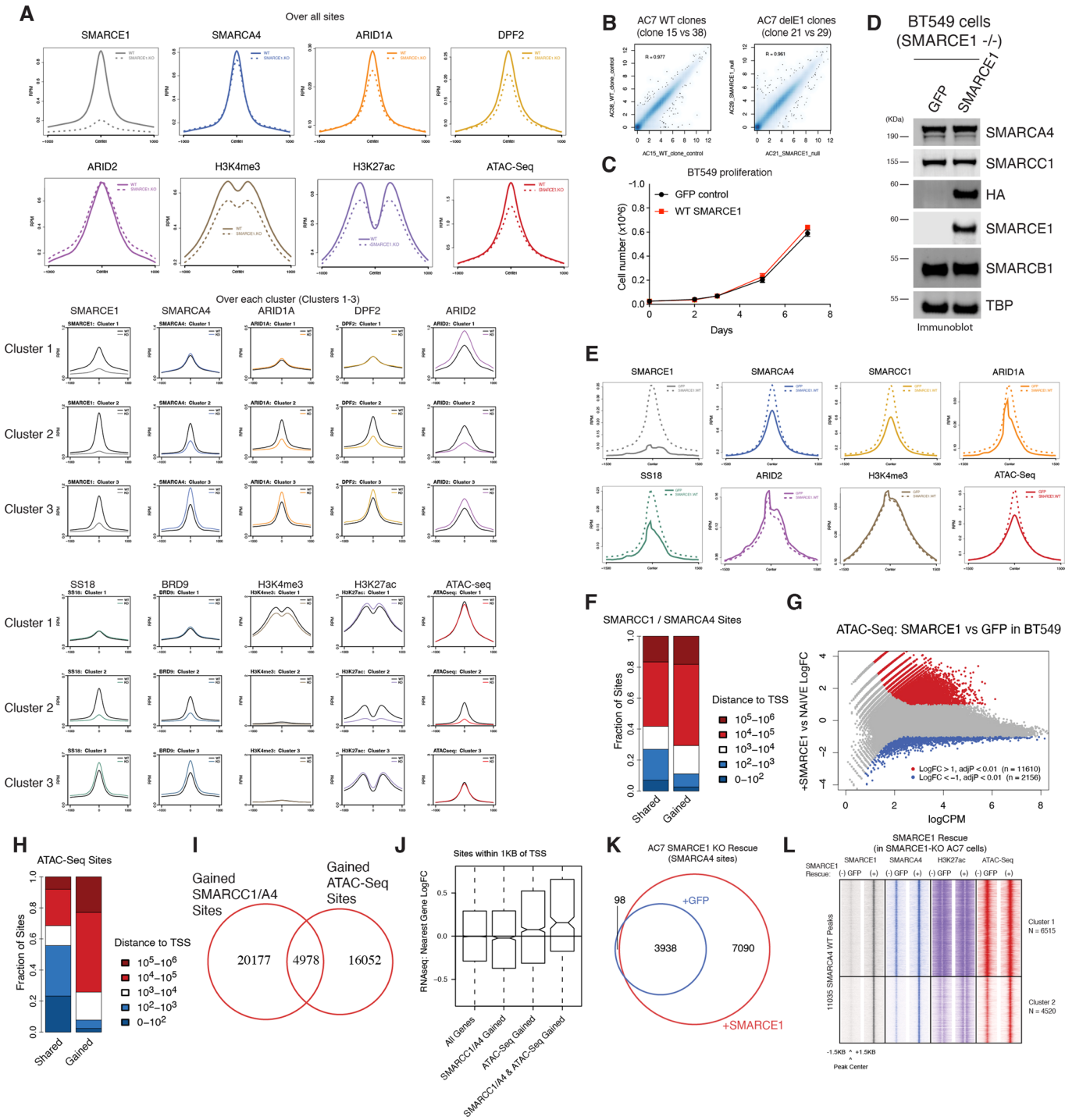

Extended Data Fig. 3 | The SMARCE1 subunit in cBAF complexes is required for cBAF-mediated enhancer accessibility. a. Top, Metaplots over all peaks from Fig. 3b for SMARCE1, SMARCA4, ARID1A, DPF2, ARID2, SS18, H3K27Ac, H3K4me3, and ATAC-seq. Solid line, wild-type AC7 cells; dashed line, SMARCE1 KO cells; Bottom, metaplots over each cluster (clusters 1–3). **b**. Correlation plots of RNA-seq data between two independent SMARCE1-KO AC7 clones. **c**. Proliferation of BT549 cells with GFP control or WT SMARCE1 rescue. **d**. Immunoblot performed on nuclear protein isolated from BT549 cells rescued with control GFP, and wild type SMARCE1. **e**. Metaplots for ChIP-seq performed on BT549 cells in naive (GFP control infected) or +SMARCE1 conditions (over all peaks from Fig. 3h). **f**. Stacked bar graph indicating distribution of shared and gained SMARCC1/SMARCA4 peaks upon SMARCE1 rescue in BT549 cells by distance to TSS. **g**. MA plot reflecting accessibility changes upon SMARCE1 rescue in BT549 cells. **h**. Stacked bar graph indicating distribution of shared and gained DNA accessibility (ATAC-seq) peaks upon SMARCE1 rescue in BT549 cells by distance to TSS. **i**. Venn Diagram reflecting overlap between gained SMARCA4/SMARCC1 merged peaks and gained ATAC-seq peaks in BT549 cells in the + SMARCE1 rescue condition. **j**. Box and whisker plot reflecting gene expression LogFC across sites indicated (gained BAF complex target sites, gained DNA accessibility sites, and BAF/accessibility dually gained sites in BT549 cells with +SMARCE1 rescue. **k**. Venn diagram of SMARCA4 sites in SMARCE1-KO AC7 cells rescued with either GFP control or WT SMARCE1. **l**. Heatmap for all merged SMARCA4 sites depicting SMARCE1, SMARCA4, H3K27Ac ChIP-seq, and ATAC-seq in SMARCE1-KO AC7 cells rescued with either GFP control or WT SMARCE1.

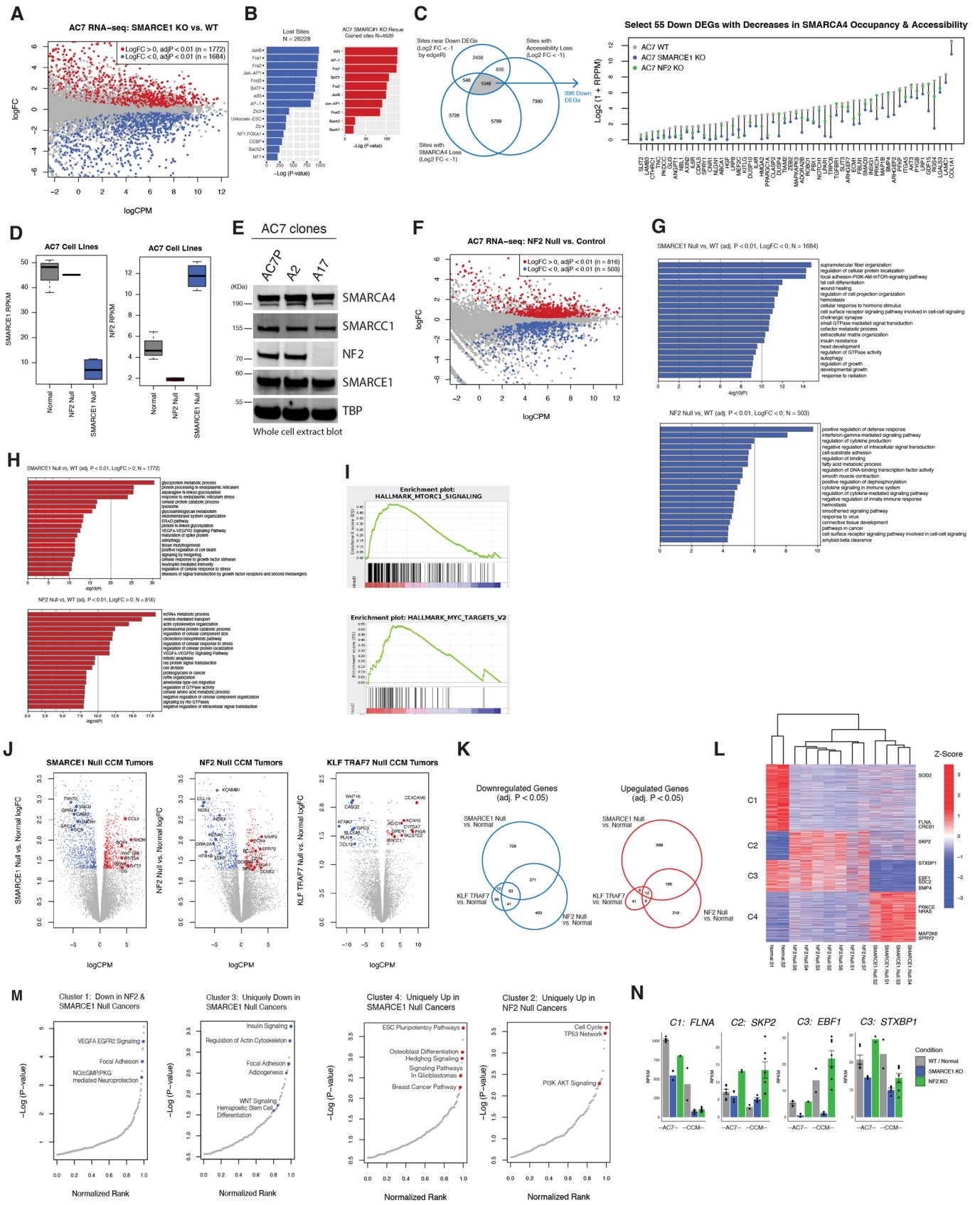

Extended Data Fig. 4 | See next page for caption.

Extended Data Fig. 4 | SMARCE1 loss alters transcriptome in SMARCE1-deficient AC7 cells and in clear cell meningioma tumors. a. MA plot showing gene expression changes upon SMARCE1 loss in AC7 cells. Red and blue dots represent genes significantly upregulated and downregulated, respectively (adj. $P < 0.01$). **b**. Motif enrichment analysis by HOMER over sites of BAF occupancy loss in SMARCE1-deficient AC7 cells and of BAF occupancy gain in SMARCE1-deficient cells rescued by WT SMARCE1. **c**. (Left) Venn diagram reflecting overlap among sites with SMARCA4 loss, sites with accessibility loss, and sites nearest to genes with significant decreases in expression in SMARCE1-deficient AC7 relative to WT (from Cluster 2 in Fig. 3b); (right) Lollipop plot displaying expression of select 55 genes downregulated in AC7 cells that are near sites with decreases in both BAF binding and accessibility. **d**. Boxplots displaying expression levels of SMARCE1 and NF2 genes in control, SMARCE1-deficient, and NF2-deficient AC7 cells (data from $n = 3$ biologically-independent cell lines, for normal and SMARCE1-null, and $n = 1$ cell line for NF2-null; center represents mean, whiskers represent 1.5*IQR, bound of box represent 25th and 75th percentiles for RPKM values). **e**. Immunoblot performed on nuclear protein isolated from NF2-deficient AC7 clones with associated control; representative of $n = 3$ experiments with similar results. **f**. MA plot showing gene expression changes upon NF2 loss in AC7 cells. Red and blue dots represent genes significantly upregulated and downregulated, respectively (adj. $P < 0.01$). **g,h**. Gene ontology analysis by Metascape on up and down DEGs (adj. $P < 0.01$) in SMARCE1-deficient and NF2-deficient AC7 cells relative to the WT condition. **i**. GSEA results displaying Hallmark MTORC1 Signaling and MYC Targets gene set enrichment for NF2 deficient AC7 cells. **j**. Volcano plots showing differentially expressed genes in SMARCE1-deficient, NF2-deficient, and KLF/TRAF7-deficient clear cell meningioma tumors relative to normal tissues. Red and blue dots represent genes significantly upregulated and downregulated DEGs, respectively (adj. $P < 0.05$). **k**. Venn diagrams reflecting overlap of upregulated and downregulated DEGs for SMARCE1-deficient, NF2-deficient, and KLF/TRAF7-deficient clear cell meningioma tumors relative to normal tissues. **l**. Heatmap of combined differentially expressed genes from tumor RNA-seq data shown in Fig. 4m. After Z-score transformation, K-means clustering was used to partition the data into 4 groups. **m**. Gene set enrichment results from hypergeometric tests (using Wikipathway MSIGDB gene set collection) from clusters from Fig. 4g. **n**. Bar plots displaying gene expression for select genes (FLNA, EBF1, STXBP1, and SKP2) in WT or normal, SMARCE1-deficient, and NF2-deficient AC7 cells and CCM tumors from clusters in Fig. 4g (Mean with error bars representing S.D. are shown for primary tumors, derived from $n = />3$ biological replicates (samples)).

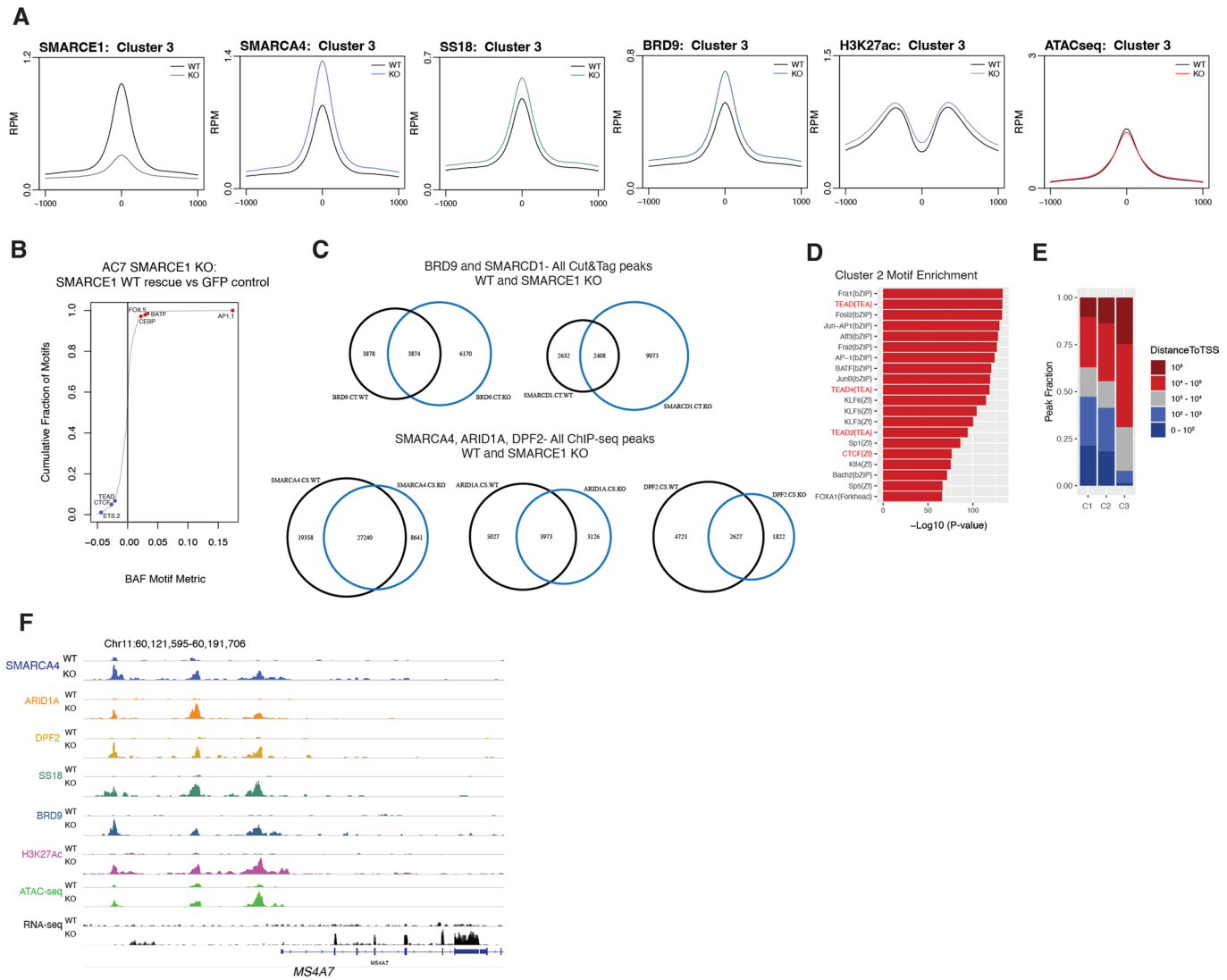

Extended Data Fig. 5 | Increased biochemical assembly and targeting of ncBAF complexes upon loss of the SMARCE1 subunit. a. Metaplots for SMARCE1, SMARCA4, SS18, BRD9, H3K27Ac, and ATAC-seq performed over Cluster 3 in Fig. 3b. **b**. ECDF plots of SMARCA4 Log2 fold change (relative to WT) as a function of motif count for 286 non-redundant transcription factor archetypes motifs over merged BAF peaks in AC7 SMARCE1-KO cells rescued with WT SMARCE1. **c**. Venn diagrams reflecting (top) all Cut&Tag peaks for BRD9 and SMARCD1 in SMARCE1 WT and KO conditions in AC7 cells; (bottom) Venn diagrams reflecting all ChIP-seq peaks for SMARCA4, ARDI1A, DPF2 in SMARCE1 WT and KO conditions in AC7 cells. **d**. HOMER motif enrichment performed on Cluster 2 (gained) sites in Fig. 5f. **e**. Distance to TSS stacked bar graphs corresponding to retained, gained, and lost clusters of SMARCD1 and BRD9 sites identified in Fig. 5f. **f**. Example tracks at the MS4A7 locus. Tracks for mSWI/SNF subunits, H3K27ac mark, as well as ATAC-seq and RNA-seq tracks are shown.

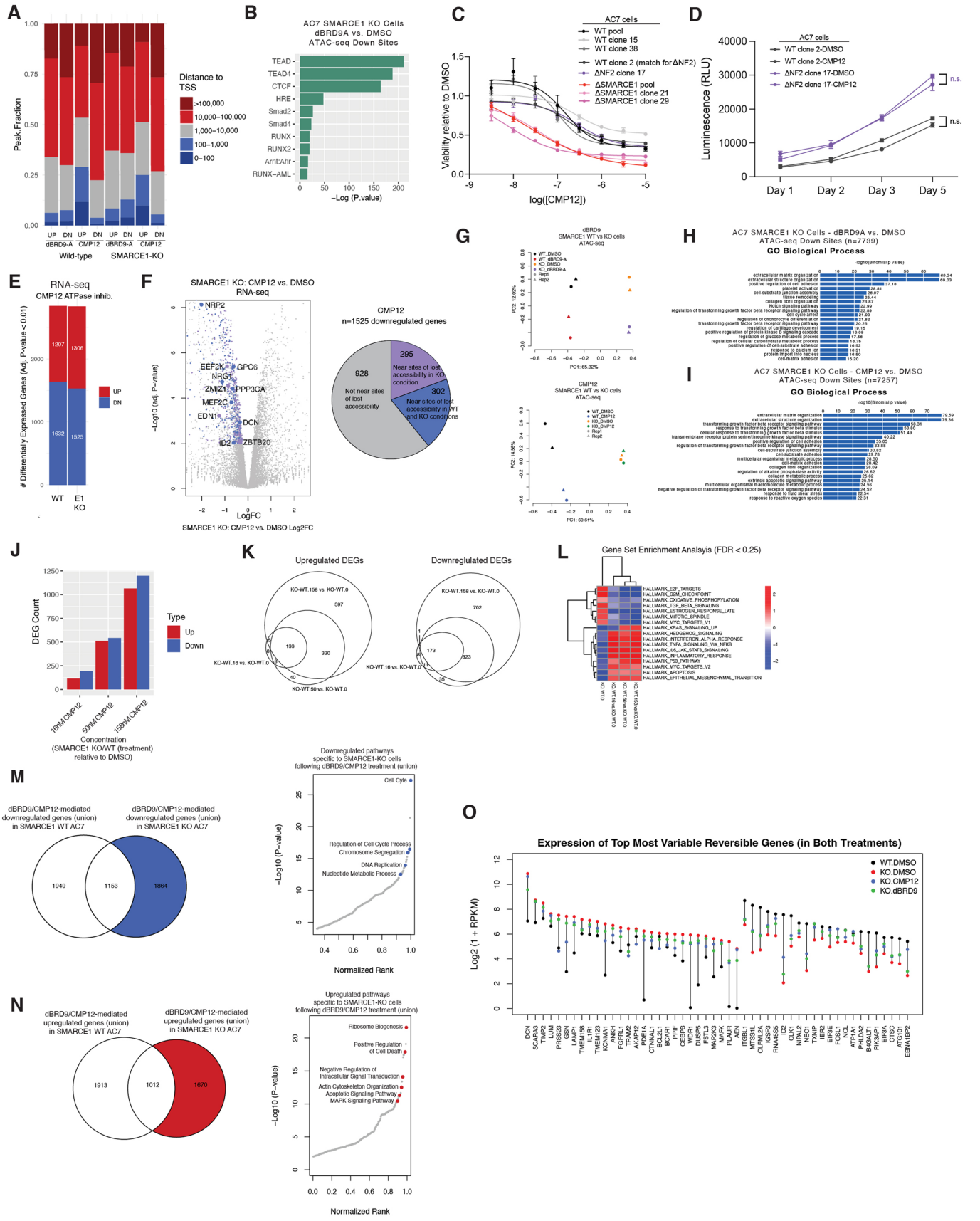

Extended Data Fig. 6 | See next page for caption.

Extended Data Fig. 6 | ncBAF inhibition as synthetic lethal strategy in SMARCE1-deficient clear cell meningioma. a. Distance to TSS stacked bar graphs for differentially accessible sites (adj $P < 0.05$) following dBRD9A and CMP12 treatment in SMARCE1-KO and WT AC7 cells. **b**. Motif enrichment analysis by HOMER over sites with accessibility loss in SMARCE1-deficient AC7 cells after dBRD9A treatment (adj $P < 0.05$). **c**. Dose response curves showing CMP12 treatments of WT, SMARCE1-KO, and NF2-KO AC-7 cell lines ($n = 2$; Mean with SD). **d**. Proliferation curves for WT and NF2-KO clones treated with 50 nM of CMP12 over the days indicated. Error bars represent S.D. of mean, and p-values derived from two-sided t test are shown (n.s., non-significant), data from $n = 3$ biologically-independent experiments. **e**. Stacked bar plots displaying numbers of differentially expressed genes after CMP12 treatment in WT and SMARCE1-deficient AC7 cells. **f**. (Left) Volcano plot showing differentially expressed genes in SMARCE1-deficient AC7 cells after CMP12 treatment relative to DMSO. Blue dots represent genes with significantly downregulated DEGs (adj. $P < 0.01$) and purple dots represent downregulated genes that map to sites with accessibility loss in the SMARCE1-deficient cells but not WT cells after dBRD9A treatment. (Right) Pie chart characterizes the distribution of downregulated genes in the SMARCE1-deficient cells after dBRD9A treatment. **g**. PCA Analysis of ATAC-seq data over merged ATAC-seq peaks for dBRD9A (top) and CMP12 (bottom) treatment in WT and SMARCE1-deficient AC7 cells. **h**, **i**. Cis-regulatory analysis by GREAT on differentially accessible sites after dBRD9A treatment (top) and CMP12 treatment (bottom) in SMARCE1-deficient AC7 cells using Go Biological Process terms. **j**. Bar plots displaying numbers of differentially expressed genes after CMP12 treatment in WT and SMARCE1-deficient AC7 cells at three concentrations relative to changes between WT and SMARCE1-deficient cells in the DMSO condition. **k**. Venn diagrams show the overlap of upregulated and downregulated DEGs between KO and WT conditions at three concentrations relative to the differences between the KO and WT in the DMSO condition. **l**. GSEA results showing gene set enrichment (using Hallmark MSIGDB gene set collection) for the KO vs. WT in DMSO comparison and across 3 concentrations of CMP12. **m**. (left) Venn diagram highlighting downregulated DEGs after dBRD9A/CMP12 treatment (union) in SMARCE1-deficient cells that are not downregulated in WT cells. (Right) Gene ontology analysis performed on genes downregulated following dBRD9A/CMP12 treatment (union) in SMARCE1-KO but not WT cells. **n**. (Left) Venn diagram highlighting upregulated DEGs after dBRD9A/CMP12 treatment (union) in SMARCE1-deficient cells that are not upregulated in WT cells. (Right) Gene ontology analysis performed on DEGs in red shaded region of Venn diagram on left. **o**. Expression of top most variable genes reversed in expression by both CMP12 and dBRD9A treatments in SMARCE1-KO cells.

nature portfolio

Corresponding author(s): Cigall Kadoch, Ph.D.

Last updated by author(s): March 22, 2022

Reporting Summary

Nature Portfolio wishes to improve the reproducibility of the work that we publish. This form provides structure for consistency and transparency in reporting. For further information on Nature Portfolio policies, see our Editorial Policies and the Editorial Policy Checklist.

Statistics

For all statistical analyses, confirm that the following items are present in the figure legend, table legend, main text, or Methods section.

n/a	Confirmed
☐	☒ The exact sample size (*n*) for each experimental group/condition, given as a discrete number and unit of measurement
☐	☒ A statement on whether measurements were taken from distinct samples or whether the same sample was measured repeatedly
☐	☒ The statistical test(s) used AND whether they are one- or two-sided *Only common tests should be described solely by name; describe more complex techniques in the Methods section.*
☒	☐ A description of all covariates tested
☒	☐ A description of any assumptions or corrections, such as tests of normality and adjustment for multiple comparisons
☐	☒ A full description of the statistical parameters including central tendency (e.g. means) or other basic estimates (e.g. regression coefficient) AND variation (e.g. standard deviation) or associated estimates of uncertainty (e.g. confidence intervals)
☐	☒ For null hypothesis testing, the test statistic (e.g. *F*, *t*, *r*) with confidence intervals, effect sizes, degrees of freedom and *P* value noted *Give P values as exact values whenever suitable.*
☒	☐ For Bayesian analysis, information on the choice of priors and Markov chain Monte Carlo settings
☒	☐ For hierarchical and complex designs, identification of the appropriate level for tests and full reporting of outcomes
☐	☒ Estimates of effect sizes (e.g. Cohen's *d*, Pearson's *r*), indicating how they were calculated

Our web collection on statistics for biologists contains articles on many of the points above.

Software and code

Policy information about availability of computer code

Data collection	Genomic samples from ChIP-Seq, Cut&Tag, ATAC-Seq, and RNA-Seq experiments were all sequenced on the Illumina Next-seq 500.
Data analysis	- Illumina NextSeq output data were demultiplexed and converted to FASTQ format using the bcl2fastq software tool (v2.20). - RNAseq reads were aligned to the hg19 genome with STAR v2.5.2b, which output gene count tables to the hg19 refFlat annotation, and ChIPseq reads were aligned with Bowtie2 v2.29 in the -k 1 reporting mode. - For the ATACseq data, quality read trimming was performed by Trimmmomatic v0.36, followed by alignment, duplicate read removal, and read quality filtering, using Bowtie2 v2.29, Picard v2.8.0, and SAMtools v0.1.19, respectively. - For the ChIPseq and ATACseq data, output BAM files were converted into BigWig track files using MACS2 and UCSC utilities in order to display coverage throughout the genome (in RPM). - For Cut and Tag libraries, the CutRunTools pipeline was leveraged to perform read trimming, quality filtering, alignment, peak calling, and track building using default parameters. - Genome_build: hg19 (GRCh37) - Supplementary_files_format_and_content: *.bw: bigWig files give the normalized coverage of DNA fragments across the genome in reads per million. - Supplementary_files_format_and_content: *.ReadsPerGene.txt: Gene count tables give raw read counts mapped to exons of given genes. - Version v2.20 (Illumina) of bcl2fastq software was used. Detailed data analysis pipeline can be found in the methods section of this study. For graphs, GraphPad Prism was used to generate all plots and graphs (i.e. proliferation and dose response); MS Excel was used to generate all (2-tailed t-test) p-values.

For manuscripts utilizing custom algorithms or software that are central to the research but not yet described in published literature, software must be made available to editors and reviewers. We strongly encourage code deposition in a community repository (e.g. GitHub). See the Nature Portfolio guidelines for submitting code & software for further information.

Data

Policy information about availability of data

All manuscripts must include a data availability statement. This statement should provide the following information, where applicable:

- Accession codes, unique identifiers, or web links for publicly available datasets
- A description of any restrictions on data availability
- For clinical datasets or third party data, please ensure that the statement adheres to our policy

All databases/datasets used in the study:
Published:
Smith, M. J. et al. Nat. Genet. 45, 295–298 (2013); PMID 23377182
Smith, M. J. et al. J. Pathol. 234, 436–440 (2014); PMID 25143307
Gerkes, E. H. et al. Neurogenetics 17, 83–89 (2016); PMID 26803492
Tauziede-Espariat, A. et al. Brain Pathol. 28, 466–474 (2018); PMID 28474749
Inoue, T. et al. Acta Neurochir. 160, 2321–2325 (2018) 30421029
Libert, D. M. et al. Ann. Diagn. Pathol. 46, 151516 (2020) 32311644
Shoakazemi, A. et al. Am. J. Med. Genet. A 185, 561–565 (2021) 33185983
Navalkele, P. et al. J. Neuropathol. Exp. Neurol. 79, 1250–1252 (2020) 33085974
Sievers, P. et al. Acta Neuropathol. 141, 281–290 (2021) 33319313

This study:
SMARCE1 mutation status (primary samples):
KLF4 p.Lys409Gln; TRAF7 p.Arg641Pro KLF4_TRAF7 missense mutation This study
KLF4 p.Lys409Gln; TRAF7 p.Asn520Ser
p.Leu425Ter NF2 loss This study
p.Glu34Serfs*6; TP53 p.Arg283Cys
p.Leu127Ter
p.Lys332Ter
p.Gln324Ter
p.Asp78Glufs*45
p.S208Rfs*26 SMARCE1 loss This study
N/A SMARCE1 loss This study
p.Arg272Glyfs*5 SMARCE1 loss Gerkes et al.2016
"Hit 1: p.(Glu125_Ala132delinsGlyLeuHisAr
gPhelleValLeu)
Hit 2: p.(Asp90Thrfs*2)" "Hit 1: partially retained copy contains amino acid inversion within HMG domain
Hit 2: allelic loss" Smith et al.2014
Normal meninges
*These data subject to controlled access (physician request), and will be made available upon request.

hg19 genome: https://www.ncbi.nlm.nih.gov/assembly/GCF_000001405.13/

For all datasets generated in this study (ChIP-seq, Cut&Tag, ATAC-seq, RNA-seq) deposited in GEO accession GSE174360, go to https://www.ncbi.nlm.nih.gov/geo/query/acc.cgi?acc=GSE174360, and see below in "Datasets".

Field-specific reporting

Please select the one below that is the best fit for your research. If you are not sure, read the appropriate sections before making your selection.

☒ Life sciences ☐ Behavioural & social sciences ☐ Ecological, evolutionary & environmental sciences

For a reference copy of the document with all sections, see nature.com/documents/nr-reporting-summary-flat.pdf

Life sciences study design

All studies must disclose on these points even when the disclosure is negative.

Sample size	Sample size was determined based on standard in the field for experimentation (n>3 replicates, where possible), and availability of (rare) primary human specimens.
Data exclusions	Following RNA extraction, five primary human meningioma samples were excluded from this study due to poor sample preservation/ poor resultant RNA quality.
Replication	All biochemical studies were performed in triplicate (n=3) or greater for all experiments. Genomic studies (ChIP-seq, RNA-seq, ATAC-seq) from cell lines were all carried out in duplicate. RNA seq from primary human samples were carried out in singlicate with multiple samples per meningioma (mutant or wild-type) subtype. All attempts at replication for data shown in the study were successful.
Randomization	There was no requirement for randomization in our experimental set up. Control of covariates was not relevant in this study given that the

Randomization	studies performed were designed to assess features across experimental groups and significance of impact of drug treatments across experimental groups (of cells, not primary samples or patients).
Blinding	Blinding was not relevant in this study; this was not a clinical study and investigators required knowledge of . Experimental set-ups were established.

Reporting for specific materials, systems and methods

We require information from authors about some types of materials, experimental systems and methods used in many studies. Here, indicate whether each material, system or method listed is relevant to your study. If you are not sure if a list item applies to your research, read the appropriate section before selecting a response.

Materials & experimental systems

n/a	Involved in the study
☐	☒ Antibodies
☐	☒ Eukaryotic cell lines
☒	☐ Palaeontology and archaeology
☒	☐ Animals and other organisms
☒	☐ Human research participants
☒	☐ Clinical data
☒	☐ Dual use research of concern

Methods

n/a	Involved in the study
☐	☒ ChIP-seq
☒	☐ Flow cytometry
☒	☐ MRI-based neuroimaging

Antibodies

Antibodies used

Primary antibodies used in this study for western blot (WB), immunoprecipitation (IP), chromatin immunoprecipitation (ChIP), and CUT&TAG:
Experiment(s), Species and Epitope, Vendor, Product #
CUT&TAG, ChIP Rabbit anti-BAF57/SMARCE1 Abcam ab70540
CUT&TAG, ChIP Rabbit anti-BRD9 Active Motif 61537
CUT&TAG, ChIP Rabbit anti-DPF2/REQ [EPR9206(B)] Abcam ab134942
CUT&TAG, ChIP Rabbit anti-Histone H3 (acetyl K27) Abcam ab4729
CUT&TAG, ChIP Rabbit anti-Histone H3 (tri methyl K4) Abcam ab8580
CUT&TAG, ChIP Rabbit anti-SMARCC1/BAF155 (D7F8S) "Cell Signaling Technology" 11956S
CUT&TAG, ChIP, IP Rabbit anti-ARID1A/BAF250A (D2A8U) "Cell Signaling Technology" 11956S
CUT&TAG, ChIP, IP Rabbit anti-ARID2 (D8D8U) "Cell Signaling Technology" 82342S
CUT&TAG, ChIP, IP Rabbit anti-SMARCA4 (EPNCIR111A) Abcam ab110641
CUT&TAG, IP Rabbit anti-IgG "Santa Cruz" sc-2027
CUT&TAG, WB Rabbit anti-SS18 (D6I4Z) "Cell Signaling Technology" 21792S
WB Mouse anti-ARID1A (C-7) "Santa Cruz" sc-373784
WB Mouse anti-ARID2 (E-3) "Santa Cruz" sc-166117
WB Mouse anti-BAF53A (E-3) "Santa Cruz" sc-137062
WB Mouse anti-GLTSCR1 (H-10) "Santa Cruz" sc-515086
WB Mouse anti-SMARCB1 (A-5) "Santa Cruz" sc-166165
WB Mouse anti-SMARCC2 (G-12) "Santa Cruz" sc-166237
WB Mouse anti-SMARCD1 (23) "Santa Cruz" sc-135843
WB Mouse anti-TBP Abcam ab51841
WB Rabbit anti-BAF180 Millipore ABE70
WB Rabbit anti-BAF57/SMARCE1 Bethyl A300-810A
WB Rabbit anti-BRD7 Bethyl A302-304A
WB Rabbit anti-DPF2 Bethyl A303-595A
WB Rabbit anti-HA-Tag (C29F4) "Cell Signaling Technology" 3724S
WB Rabbit anti-SMARCC1 (H-76) "Santa Cruz" sc-10756
WB, IP Mouse anti-SMARCA4 (G-7) "Santa Cruz" sc-17796
WB, IP Rabbit anti-BRD9 Bethyl A303-781A

Secondary Antibodies:
WB secondary IRDye 680RD Goat anti-Rabbit IgG (H + L) Li-Cor Biosciences 925-68071
WB secondary IRDye 800CW Donkey anti-Mouse IgG (H + L) Li-Cor Biosciences 925-32212

Validation

All antibodies above were validated by the commercial vendor (see catalog numbers for each and validation on respective websites), as well as routinely in our laboratory (using genetic KO cell lines).

Eukaryotic cell lines

Policy information about cell lines

Cell line source(s)

HEK-293T (Human; ATCC, ACS-4500)
BT549 (Human; ATCC, HTB-122)

	AC7 cell lines (Human; AC-007-hTERT, derived from a meningioma patient expressing wild-type levels of NF2, were a generous gift from Dr. Vijaya Ramesh (Massachusetts General Hospital, Boston, MA).
Authentication	Cell SNP profiling and fingerprinting was performed on HEK 293T and BT549, both of which were freshly purchased for this study (commercially available). SNP profiling was performed for AC7 cells, a well-established human arachnoid model used to model meningioma.
Mycoplasma contamination	All cell lines used in this study routinely tested negative for mycoplasma contamination, in accordance with lab protocol.
Commonly misidentified lines (See ICLAC register)	No cell lines used in this study are known to be commonly misidentified lines.

ChIP-seq

Data deposition

☒ Confirm that both raw and final processed data have been deposited in a public database such as GEO.

☒ Confirm that you have deposited or provided access to graph files (e.g. BED files) for the called peaks.

Data access links *May remain private before publication.*	To review GEO accession GSE174360, go to https://www.ncbi.nlm.nih.gov/geo/query/acc.cgi?acc=GSE174360 Reviewer token: mjcxyeauhvonxkf
Files in database submission	ATACseq.AC7.ATAC.SMARCE1_KO.Rep1 ATACseq.AC7.ATAC.SMARCE1_KO.Rep2 ATACseq.AC7.ATAC.SMARCE1_KO.100nM.CMP12.Rep1b ATACseq.AC7.ATAC.SMARCE1_KO.100nM.CMP12.Rep2b ATACseq.AC7.ATAC.SMARCE1_KO.2uM.dBRDA.Rep1b ATACseq.AC7.ATAC.SMARCE1_KO.2uM.dBRDA.Rep2b ATACseq.AC7.ATAC.SMARCE1_KO.DMSO.Rep1 ATACseq.AC7.ATAC.SMARCE1_KO.DMSO.Rep1b ATACseq.AC7.ATAC.SMARCE1_KO.DMSO.Rep2 ATACseq.AC7.ATAC.SMARCE1_KO.DMSO.Rep2b ATACseq.AC7.ATAC.WT.100nM.CMP12.Rep1b ATACseq.AC7.ATAC.WT.100nM.CMP12.Rep2b ATACseq.AC7.ATAC.WT.2uM.dBRDA.Rep1b ATACseq.AC7.ATAC.WT.2uM.dBRDA.Rep2b ATACseq.AC7.ATAC.WT.DMSO.Rep1 ATACseq.AC7.ATAC.WT.DMSO.Rep1b ATACseq.AC7.ATAC.WT.DMSO.Rep2 ATACseq.AC7.ATAC.WT.DMSO.Rep2b ATACseq.AC7.ATAC.WT.Rep1 ATACseq.AC7.ATAC.WT.Rep2 ATACseq.BT549.ATAC.GFP.Rep1 ATACseq.BT549.ATAC.GFP.Rep2 ATACseq.BT549.ATAC.SMARCE1.WT.Rep1 ATACseq.BT549.ATAC.SMARCE1.WT.Rep2 ChIPseq.AC7.ARID1A.SMARCE1_KO ChIPseq.AC7.ARID1A.WT ChIPseq.AC7.BRD9.SMARCE1_KO ChIPseq.AC7.BRD9.WT ChIPseq.AC7.CTCF.SMARCE1_KO ChIPseq.AC7.CTCF.WT ChIPseq.AC7.DPF2.SMARCE1_KO ChIPseq.AC7.DPF2.WT ChIPseq.AC7.H3K27Ac.SMARCE1_KO ChIPseq.AC7.H3K27Ac.WT ChIPseq.AC7.H3K4me3.SMARCE1_KO ChIPseq.AC7.H3K4me3.WT ChIPseq.AC7.SMARCE1.SMARCE1_KO ChIPseq.AC7.SMARCE1.WT ChIPseq.AC7.Input.SMARCE1_KO ChIPseq.AC7.Input.WT ChIPseq.AC7.POL2.SMARCE1_KO ChIPseq.AC7.POL2.WT ChIPseq.AC7.SMARCA4.SMARCE1_KO ChIPseq.AC7.SMARCA4.WT ChIPseq.AC7.SS18.SMARCE1_KO ChIPseq.AC7.SS18.WT ChIPseq.BT549.ARID1A.GFP ChIPseq.BT549.ARID1A.SMARCE1.WT ChIPseq.BT549.ARID2.GFP ChIPseq.BT549.ARID2.SMARCE1.WT ChIPseq.BT549.H3K27ac.GFP

ChIPseq.BT549.H3K27ac.SMARCE1.WT
ChIPseq.BT549.H3K4me3.GFP
ChIPseq.BT549.H3K4me3.SMARCE1.WT
ChIPseq.BT549.Input.DOX.N102.V5.SMARCE1
ChIPseq.BT549.Input.Naïve
ChIPseq.BT549.SMARCA4.DOX.N102.V5.SMARCE1
ChIPseq.BT549.SMARCA4.Naïve
ChIPseq.BT549.SMARCC1.DOX.N102.V5.SMARCE1
ChIPseq.BT549.SMARCC1.Naïve
ChIPseq.BT549.SMARCE1.GFP
ChIPseq.BT549.SMARCE1.SMARCE1.WT
ChIPseq.BT549.SS18.GFP
ChIPseq.BT549.SS18.SMARCE1.WT
CutAndTag.AC7.250A.SMARCE1_KO
CutAndTag.AC7.250A.WT
CutAndTag.AC7.ACTL6A.SMARCE1_KO
CutAndTag.AC7.ACTL6A.WT
CutAndTag.AC7.BRG1.SMARCE1_KO
CutAndTag.AC7.BRG1.WT
CutAndTag.AC7.DPF2.SMARCE1_KO
CutAndTag.AC7.DPF2.WT
CutAndTag.AC7.SMARCE1.SMARCE1_KO
CutAndTag.AC7.SMARCE1.WT
CutAndTag.AC7.IgG.WT
CutAndTag.AC7.SMARCB1.SMARCE1_KO
CutAndTag.AC7.SMARCB1.WT
CutAndTag.AC7.SMARCC1.SMARCE1_KO
CutAndTag.AC7.SMARCC1.WT
CutAndTag.AC7.SMARCD1.SMARCE1_KO
CutAndTag.AC7.SMARCD1.WT
CutAndTag.AC7.SS18.SMARCE1_KO
CutAndTag.AC7.SS18.WT
RNAseq.AC7.RNA.Clone15.WT.Control.Rep1
RNAseq.AC7.RNA.Clone15.WT.Control.Rep2
RNAseq.AC7.RNA.Clone17.WT.Control.Rep1
RNAseq.AC7.RNA.Clone17.WT.Control.Rep2
RNAseq.AC7.RNA.Clone21.SMARCE1.Null.Rep1
RNAseq.AC7.RNA.Clone21.SMARCE1.Null.Rep2
RNAseq.AC7.RNA.Clone29.SMARCE1.Null.Rep1
RNAseq.AC7.RNA.Clone29.SMARCE1.Null.Rep2
RNAseq.AC7.RNA.Clone38.WT.Control.Rep1
RNAseq.AC7.RNA.Clone38.WT.Control.Rep2
RNAseq.AC7.RNA.NF2.Null.Rep1
RNAseq.AC7.RNA.NF2.Null.Rep2
RNAseq.AC7.RNA.Parental.Rep1
RNAseq.AC7.RNA.Parental.Rep2
RNAseq.AC7.RNA.SMARCE1_KO.100nM.CMP12.Rep1b
RNAseq.AC7.RNA.SMARCE1_KO.100nM.CMP12.Rep2b
RNAseq.AC7.RNA.SMARCE1_KO.168nM.CMP12.Rep1
RNAseq.AC7.RNA.SMARCE1_KO.168nM.CMP12.Rep2
RNAseq.AC7.RNA.SMARCE1_KO.16nM.CMP12.Rep1
RNAseq.AC7.RNA.SMARCE1_KO.16nM.CMP12.Rep2
RNAseq.AC7.RNA.SMARCE1_KO.2000nM.dBRD9A.Rep1b
RNAseq.AC7.RNA.SMARCE1_KO.2000nM.dBRD9A.Rep2b
RNAseq.AC7.RNA.SMARCE1_KO.50nM.CMP12.Rep1
RNAseq.AC7.RNA.SMARCE1_KO.50nM.CMP12.Rep2
RNAseq.AC7.RNA.SMARCE1_KO.DMSO.Rep1
RNAseq.AC7.RNA.SMARCE1_KO.DMSO.Rep1b
RNAseq.AC7.RNA.SMARCE1_KO.DMSO.Rep2
RNAseq.AC7.RNA.SMARCE1_KO.DMSO.Rep2b
RNAseq.AC7.RNA.WT.100nM.CMP12.Rep1b
RNAseq.AC7.RNA.WT.100nM.CMP12.Rep2b
RNAseq.AC7.RNA.WT.168nM.CMP12.Rep1
RNAseq.AC7.RNA.WT.168nM.CMP12.Rep2
RNAseq.AC7.RNA.WT.16nM.CMP12.Rep1
RNAseq.AC7.RNA.WT.16nM.CMP12.Rep2
RNAseq.AC7.RNA.WT.2000nM.dBRD9A.Rep1b
RNAseq.AC7.RNA.WT.2000nM.dBRD9A.Rep2b
RNAseq.AC7.RNA.WT.50nM.CMP12.Rep1
RNAseq.AC7.RNA.WT.50nM.CMP12.Rep2
RNAseq.AC7.RNA.WT.DMSO.Rep1
RNAseq.AC7.RNA.WT.DMSO.Rep1b
RNAseq.AC7.RNA.WT.DMSO.Rep2
RNAseq.AC7.RNA.WT.DMSO.Rep2b
RNAseq.BT549.RNA.GFP.Rep1
RNAseq.BT549.RNA.GFP.Rep2

RNAseq.BT549.RNA.SMARCE1.WT.Rep1
RNAseq.BT549.RNA.SMARCE1.WT.Rep2
RNAseq.CCM.RNA.KLF4.TRAF7.Null.Tumor.Sample1
RNAseq.CCM.RNA.KLF4.TRAF7.Null.Tumor.Sample2
RNAseq.CCM.RNA.NF2.Null.Tumor.Sample1
RNAseq.CCM.RNA.NF2.Null.Tumor.Sample2
RNAseq.CCM.RNA.NF2.Null.Tumor.Sample3
RNAseq.CCM.RNA.NF2.Null.Tumor.Sample4
RNAseq.CCM.RNA.NF2.Null.Tumor.Sample5
RNAseq.CCM.RNA.NF2.Null.Tumor.Sample6
RNAseq.CCM.RNA.NF2.Null.Tumor.Sample7
RNAseq.CCM.RNA.Normal.Brain.Tissue.Sample1
RNAseq.CCM.RNA.Normal.Brain.Tissue.Sample2
RNAseq.CCM.RNA.SMARCE1.Null.Tumor.Sample1
RNAseq.CCM.RNA.SMARCE1.Null.Tumor.Sample2
RNAseq.CCM.RNA.SMARCE1.Null.Tumor.Sample3
RNAseq.CCM.RNA.SMARCE1.Null.Tumor.Sample4
ATACseq.AC7.SMARCE1.KO.ATAC.GFP.Rep1
ATACseq.AC7.SMARCE1.KO.ATAC.GFP.Rep2
ATACseq.AC7.SMARCE1.KO.ATAC.SMARCE1.WT.Rep1
ATACseq.AC7.SMARCE1.KO.ATAC.SMARCE1.WT.Rep2
ChIPseq.AC7.SMARCE1.KO.GFP.H3K27ac
ChIPseq.AC7.SMARCE1.KO.GFP.Input May 12, 2024
ChIPseq.AC7.SMARCE1.KO.GFP.SMARCA4
ChIPseq.AC7.SMARCE1.KO.GFP.SMARCE1
ChIPseq.AC7.SMARCE1.KO.SMARCE1.WT.H3K27ac
ChIPseq.AC7.SMARCE1.KO.SMARCE1.WT.Input
ChIPseq.AC7.SMARCE1.KO.SMARCE1.WT.SMARCA4
ChIPseq.AC7.SMARCE1.KO.SMARCE1.WT.SMARCE1

Genome browser session
(e.g. UCSC)

IGV was used to visualize tracks (https://igv.org/app).

Methodology

Replicates

For ChIP seq and Cut&Tag, multiple epitopes against the mSWI/SNF complexes were utilized to serve as duplicate for complex localization across the genome.

Sequencing depth

Minimum mapped reads per experiment type:
ChIP seq: 40M per sample
Cut & Tag: 8M per sample

Antibodies

Rabbit anti-BAF57/SMARCE1 Abcam ab70540
Rabbit anti-BRD9 Active Motif 61537
Rabbit anti-DPF2/REQ [EPR9206(B)] Abcam ab134942
Rabbit anti-Histone H3 (acetyl K27) Abcam ab4729
Rabbit anti-Histone H3 (tri methyl K4) Abcam ab8580
Rabbit anti-SMARCC1/BAF155 (D7F8S) "Cell Signaling Technology" 11956S
Rabbit anti-ARID1A/BAF250A (D2A8U) "Cell Signaling Technology" 11956S
Rabbit anti-ARID2 (D8D8U) "Cell Signaling Technology" 82342S
Rabbit anti-SMARCA4 (EPNCIR111A) Abcam ab110641

All experiments used 2-3ug of antibody for protein capture.

Peak calling parameters

ChIP-Seq reads were aligned with Bowtie2 v2.29 in the -k 1 reporting mode, and narrow peaks were called with the MACS2 v2.1.1 software using a q-value cutoff of 0.001.

Data quality

To assess quality enrichment across the genome, all ChIP-seq samples received 20ng of spike-in Drosophila chromatin (Active Motif), and 2µg spike-in antibody (Active Motif) for normalization post sequencing. On average, we obtained 12,000 peaks for mSWI/SNF subunits and 50,000+ peaks for chromatin mark ChIP seqs.

Software

- bcl2fastq conversion software to demultiplex sequencing datasets (v2.20)
- Bowtie2 v2.29 to align demultiplexed data to the genome
- MACS2 v2.1.1 to call narrow peaks
- deepTools v2.5.3 to generate tracks
- MACS2 and UCSC utilities were to convert output BAM files into BigWig files
- ngsplot v2.63 to generate heatmaps and metaplots
- R package, ChIPpeakAnno v3.17.0 to visualize peak overlaps, and the Bedtools multiIntersectBed
- LOLA v1.12.0 and HOMER v4.9 to carry out transcription factor enrichment and motif analyses respectively
- GREAT and chromVAR to identify motif enrichment over sites of variable accessibility or chromatin factor occupancy
- IGV-2.9.4 to display tracks

Additional in-house motif enrichement analys of ChIP set datasets are described in the method section.